

Layered Double Hydroxide Materials: Assembly and Photofunctionality

Rui Tian, Dongpeng Yan, and Min Wei

Contents

1	Introduction	3
2	Optical Properties of LDHs	4
3	Luminescent Properties of LDHs Nanoparticles	6
3.1	Defect-Induced Luminescence	6
3.2	Rare-Earth-Doped Luminescence	7
4	LDH-Based UV-Shielding Materials and the Applications	8
4.1	Introduction of UV Light and UV-Shielding Materials	8
4.2	UV-Shielding Properties of LDHs	8
4.3	Host–Guest Interaction and UV-Shielding Performances	10
4.4	Application of LDH-Based UV-Shielding Materials in Polypropylene and Asphalt	13
5	LDH-Based IR Absorption Materials and the Application	17
5.1	Introduction of IR Absorption Materials	17
5.2	IR Absorption Properties of LDHs	17
5.3	Intercalation and Performances of LDH-Based IR Absorption Materials	19
5.4	Application of LDH-Based IR Absorption Materials	22
6	Fabrication and Application of LDH-Based Host–Guest Luminescent Materials	24
6.1	The Basic Guest Units of LDH-Based Photofunctional Materials	25
6.2	Fabrication of LDH-Based Photofunctional Material	25
6.3	Adjusting Photofunctionalities of LDH-Based Materials	38
7	Conclusion and Outlook	63
	References	64

R. Tian • M. Wei

State Key Laboratory of Chemical Resource Engineering, Beijing University of Chemical
Technology, Beijing 100029, P. R. China

D. Yan (✉)

State Key Laboratory of Chemical Resource Engineering, Beijing University of Chemical
Technology, Beijing 100029, P. R. China

College of Chemistry, Beijing Normal University, Beijing 100875, P. R. China

e-mail: yandp@mail.buct.edu.cn; yandp@bnu.edu.cn

Abstract As a large type of inorganic layered compounds with diversity of composition in host layer and interlayer anions, layered double hydroxides (LDHs) have been intensively studied toward construction of advanced photofunctional materials. In this chapter, the optical properties of LDH materials and related potential applications—mainly involving the functionalities of LDH layers (such as tunable color, infrared radiation (IR) absorption, and ultraviolet (UV) shielding)—will be described firstly. Then, we will review the development of intercalated luminescent materials by adjusting both the host layer and guest molecules, in which the static and dynamic photofunctional modulations have been focused. Due to the host–guest and guest–guest interaction, fluorescence properties of composites can be effectively altered, and intelligent materials with stimuli-responsive performance can be further obtained. Finally, perspectives on the future development of LDH-based solid-state luminescent materials are addressed.

Keywords Assembly • Layered double hydroxides • Luminescence • Sensor • UV shielding

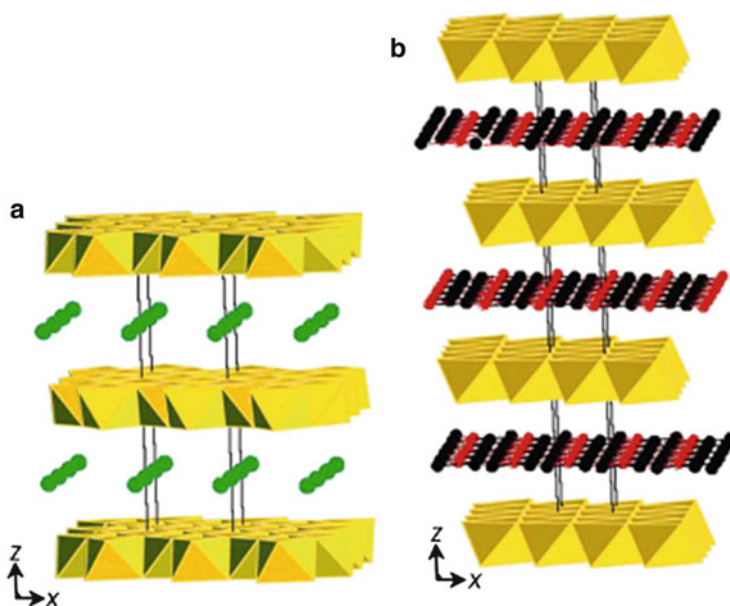
Abbreviations

AFM	Atomic force microscopy
CL	Chemiluminescence
ECL	Electrochemiluminescence
EDTA	Ethylenediaminetetraacetic acid
EL	Electroluminescence
FRET	Förster resonance energy transfer
HMIs	Heavy metal ions
IR	Infrared radiation
LDHs	Layered double hydroxides
LDPE	Low-density polyethylene
LED	Light-emitting diode
MMO	Mixed metal oxide
PL	Photoluminescence
RH	Relative humidity
SEM	Scanning electron microscopy
SNAS	Separate nucleation and aging steps
TEM	Transmission electron microscopy
UTF	Ultrathin film
UV-Vis	Ultraviolet-visible
VOCs	Volatile organic compounds
XRD	X-ray diffraction

1 Introduction

Layered double hydroxides (LDHs) are one type of anionic clay materials, also known as hydrotalcite compound [1, 2]. The basic structure of LDHs is derived from the brucite with edge-sharing $M(OH)_6$ octahedra, in which a fraction of the divalent cations are substituted by trivalent cations in the layer and the positive charges can be balanced by anions within the hydrated interlayer galleries [3–5]. For the common binary LDHs, the general formula can be expressed as $[M^{2+}_{1-x}M^{3+}_x(OH)_2] (A^{n-})_{x/n} \cdot mH_2O$, with tunable composition and relative proportions for both di- and trivalent cations as well as interlayer ions [6–8]. This versatility gives rise to a large amount of LDH-based materials with variable functionalities due to the exchange of interlayer ions and diverse properties from different elemental compositions and charge densities of host layers. The structures of LDHs have been comprehensively studied and introduced in several previous literatures [9–11], and the models for typical packing fashions (3R and 2H) of LDHs are illustrated in Scheme 1 [12].

During last few decades, LDHs have received much attention in the fields of catalysis [13], separation processes [14], photochemical cell [15], and drug carrier [16]. Moreover, based on the tunable host layer and interlayer guest molecules, the optical/luminescent properties have also been largely investigated, and a number of photofunctional materials have been developed [17]. Due to the rapid development in the design and fabrication of LDH-based photo-related materials, it is timely and



Scheme 1 Typical models of LDHs structures with two packing fashions: (a) 2H; (b) 3R [12]

necessary to summarize recent progress in this area and thus hopefully stimulate the construction of new types of layered photofunctional materials.

2 Optical Properties of LDHs

Due to different photo-absorption characteristics of the metal ions in the LDH layers, the powdered LDH materials can present different colors under daylight. Moreover, the nontransparent LDH powders can be further fabricated into continuous self-supporting transparent films through solvent evaporation or spin-coating method. The resulting films usually exhibit oriented (00 l) reflection due to the edge-edge interaction between the adjacent LDH particles. For example, alkoxide-intercalated LDHs have been synthesized in a nonaqueous media (methanol), and the hydrolysis of these LDH derivatives resulted in a colloidal LDH suspension which can be used as a precursor for the formation of continuous transparent films via solvent evaporation [18, 19]. For another example, the fabrication of oriented LDHs films without organic solvents has been attempted, and separate nucleation and aging steps (SNAS) were adopted as a main method [20]. Due to the uniform and small crystal size (about 40 nm) of the LDH platelets, both the face-to-face and edge-to-edge interactions occur between individual LDH platelets, which facilitate the formation of densely packed c -oriented LDH film [21]. The obtained films were sufficiently thick and mechanically robust and maintained good optical transparency as well as uniform colors for ZnAl-NO₃, NiAl-NO₃, and ZnAl-Tb-EDTA (EDTA, ethylenediaminetetraacetic acid) samples (Fig. 1). Moreover, Zhang [22] has fabricated oriented LDH films by a spin-coating method, and the as-prepared

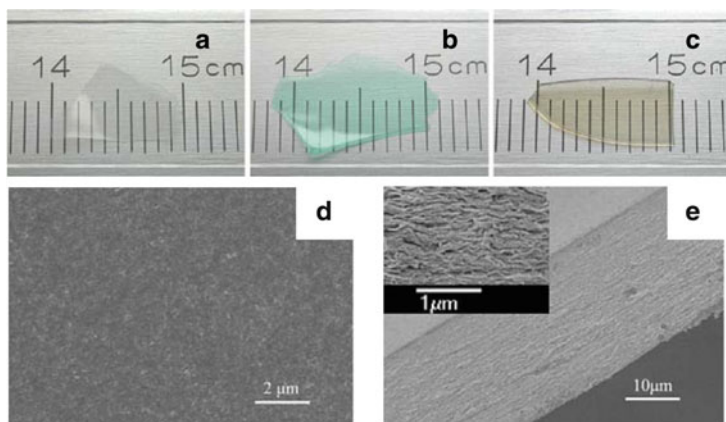


Fig. 1 Photographs of transparent self-supporting LDH films of (a) ZnAl-NO₃, (b) NiAl-NO₃, (c) ZnAl-Tb(EDTA) (the ruler with centimetre scale lies behind the films), and SEM images of ZnAl-NO₃: (d) top view and (e) edge view with a high-resolution image of this structure shown in the inset image [21]

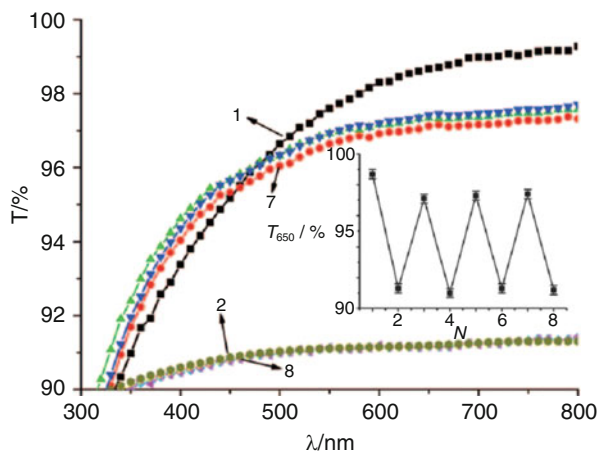


Fig. 2 UV-Vis transmittance spectra of the MMO_{10} film (1, 3, 5, 7) and the rehydrated LDH film (2, 4, 6, 8). The inset shows the transmittance at 650 nm T_{650} as a function of cycle number n ; cycling occurs between MMO and LDH films [23]

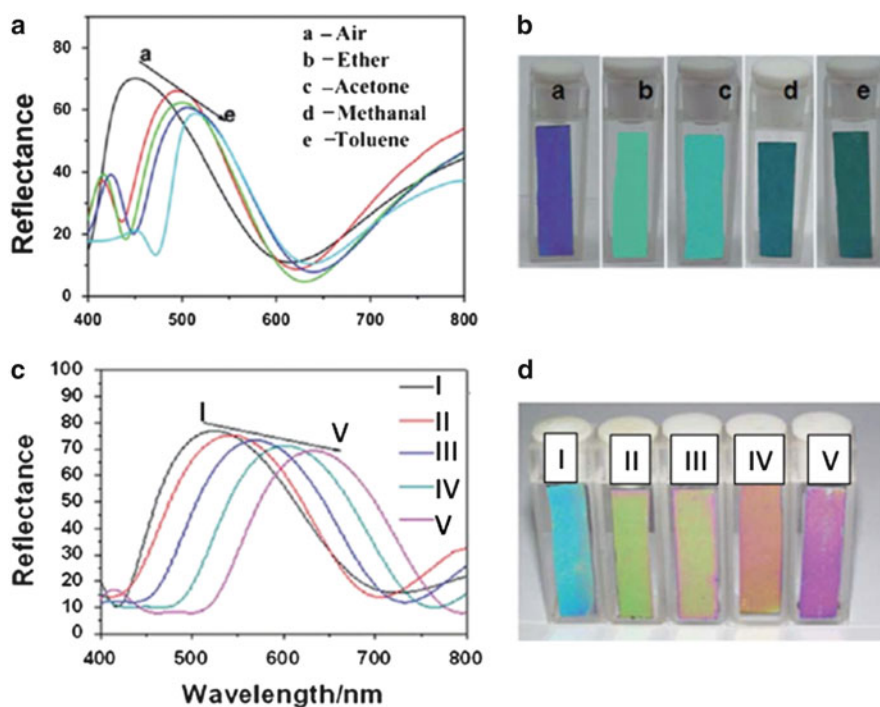


Fig. 3 Response of the $(\text{MMO-TiO}_2)_6\text{IDPC}$ toward different VOCs and RH: (A) reflectance spectra and (B) photographs in air (a) and various VOCs: (b) ether, (c) acetone, (d) methanal, and (e) toluene; (C) reflectance spectra and (D) photographs of color variation (I–V: 5 %, 30 %, 54 %, 75 %, and 85 %, respectively) [24]

films displayed good uniformity and compact structure composed of LDH platelets stacked parallel to the substrate surface.

The calcinations of LDH materials can form mixed metal oxide (MMO) with diverse optical properties compared with the pristine LDHs. Han et al. [23] have studied the optical antireflection (AR) performance of MMO through calcinations of LDHs. Figure 2 shows the changes of transmittance by the reconstruction effect of LDH materials through recycling the calcination–rehydration procedure. These AR properties were generated by the transformation between porous (MMO film) and nonporous state (LDH film), and this phenomenon makes the MMO film an effective candidate for erasable AR coatings. Furthermore, MMO-TiO₂ one-dimensional photonic crystals (1DPC) can be fabricated through deposition of LDHs and TiO₂, followed by calcination [24]. The porous structure of MMO enabled the adsorption of volatile gas or water molecule in the mesopores of the MMO-TiO₂ structure, which results in the change of optical refractive index (Fig. 3). Thus, this system can serve as a colorimetric sensor for the detection of volatile organic compounds (VOCs) or relative humidity (RH).

3 Luminescent Properties of LDHs Nanoparticles

3.1 Defect-Induced Luminescence

Several observations have proven that the pristine LDH particles and colloids can exhibit well-defined luminescence. For example, the excitation and emission spectrum of Zn-Al-LDH has been recorded in Fig. 4 [25], and emission in the 350–550 nm can be observed. The basic mechanisms for the luminescence of the LDH colloids are attributed to the numerous surface defects of LDH nanocrystals. These surface defects can act as traps which are beneficial to the recombination of excited electrons and holes, and thus, obvious luminescence can be observed. In addition, the effects of the surface charge density (e.g., the ratio of Zn to Al) on the photoluminescence (PL) have been investigated. Figure 4 shows that higher Zn/Al ratio resulted in a stronger PL intensity, that is, different surface charge density may largely influence the PL intensity of LDH colloids. In addition, fluorescence properties of MgAl-LDHs have also been studied, and influence of MgAl-LDHs with different platelet size has been considered. The results showed that LDHs with higher specific surface areas may result in more surface defects and stronger fluorescence intensity [26].

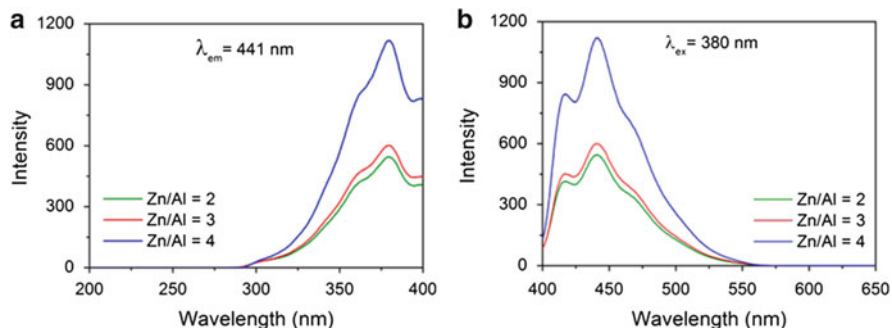


Fig. 4 Effect of Zn/Al ratio on (a) excitation and (b) emission spectra for the colloids of the pristine Zn–Al-LDHs [25]

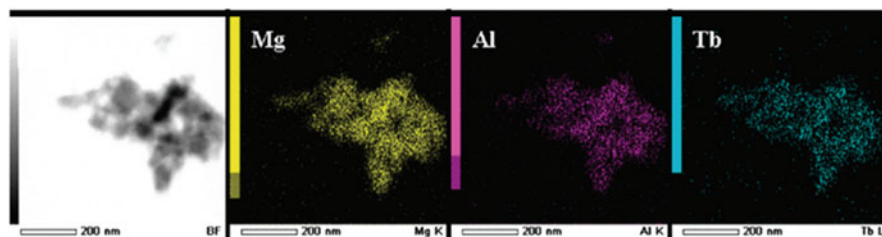


Fig. 5 TEM images and the corresponding EDS images of Mg, Al, and Tb elements in Tb³⁺ doped LDHs [29]

3.2 Rare-Earth-Doped Luminescence

One of the most striking features of LDHs is their versatility of composition, and thus, numerous metal cations can be accommodated in the host layer. It was reported that some rare-earth ions, such as lanthanide Tb³⁺, Eu³⁺, and Nd³⁺, can be doped into the octahedral lattice of the brucite-like layer [27, 28]. Incorporation of Tb³⁺ has been achieved by coprecipitation method under ambient conditions [29]. Figure 5 shows the homogeneous distribution of Tb³⁺ in the lattice of LDH layers regardless of the large ionic size of Tb³⁺, and up to 19 wt% of Tb³⁺ can be incorporated. This Tb³⁺-doped LDH presents strong luminescence in the green region due to the intra electron transition of Tb³⁺. Additionally, the photosensitizer could also be incorporated into the interlayer of rare-earth-doped LDHs to obtain an advanced performance. For example, Förster resonance energy transfer (FRET) process could occur between the interlayer guest and doped ions in the host layer of LDHs [30–32], which leads to enhanced fluorescence.

4 LDH-Based UV-Shielding Materials and the Applications

4.1 Introduction of UV Light and UV-Shielding Materials

UV light possesses the shortest wavelength in the solar spectrum, and it takes up about 8 % of the total solar energy. UV radiation includes UVC (220–290 nm), UVB (290–320 nm), and UVA (320–400 nm). Among them, UVC region is always absorbed by ozonosphere, and UVA and UVB in the range of 290–400 nm could reach the earth's surface. The UV light presents high energy which has severe damages to the environment and human health [33]. Some diseases, sunburn, acceleration of aging, and even cancer can be triggered due to the damage of skin fibers, proteins, and nucleic acids. And the commonly used organic materials (such as polypropylene, asphalt, rubber, and paints) are easy to degrade under the high energy UV light as a result of the covalent bonds breakage (e.g., C–H, C–C, C–Cl) [34]. Therefore, the shielding of UV irradiation is of great importance in our daily life.

UV-shielding materials could be classified into organic, inorganic, and organic/inorganic composites. The main organic UV absorbents include benzotriazole, benzophenone, salicylic acid, and esters; the shielding mechanism is the UV-induced molecular rearrangement, leading to the release of the absorbed energy [35, 36]. The inorganic UV blocking materials contain TiO₂, ZnO, CaCO₃, French chalk, and LDHs, and they are commonly dispersed into organic or inorganic materials to form organic/inorganic composites with enhanced UV-shielding performances [37, 38].

4.2 UV-Shielding Properties of LDHs

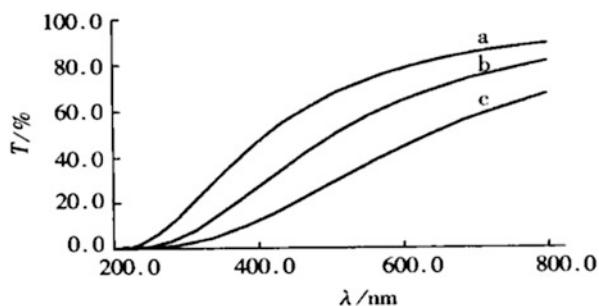
4.2.1 Scattering Effect of LDH Particles

According to the Lambert–Beer's law, the particle size severely affects the scattering and reflection effects of UV light. Xing et al. [38, 39] have prepared Zn-Al-LDHs through separate nucleation and aging steps (SNAS) at different temperatures, and the influences of particle sizes on the UV blocking properties have been investigated. The particle sizes calculated from XRD patterns via Scherrer expression are shown in Table 1. The results show that with increase of aging temperature, the particle size of LDHs increases in both *a* and *c* directions.

The suspension of ZnAl-CO₃-LDHs with different aging temperature and particle size can be obtained by dispersing the LDHs into water at 0.02 wt%, and their UV–Vis transmittance curves are shown in Fig. 6. With the increase of aging temperature, the UV-shielding performances increased obviously. In order to investigate the exact relation between particle size and UV-shielding performance,

Table 1 Particle sizes of LDHs at different aging temperatures [39]

Aging temperature (°C)	60	80	100
Particle size in <i>a</i> direction D_a (nm)	37.227	39.178	41.806
Particle size in <i>c</i> direction D_c (nm)	25.318	34.097	42.662

**Fig. 6** UV-Vis transmittance curves of suspension of ZnAl-CO₃-LDHs with different aging temperature: (a) 60 °C, (b) 80 °C, and (c) 100 °C [39]**Table 2** Threshold values of particle size in *a* and *c* directions at different wavelengths [39]

Wavelength (nm)	Threshold value in <i>a</i> direction	Threshold value in <i>c</i> direction
290	32.92	9.73
320	33.77	12.79
400	34.77	16.47
600	35.56	19.35
800	35.79	20.22

the absorbance and transmittance values are analyzed at different wavelengths, and the threshold values for UV shielding at different wavelengths are shown in Table 2. It can be known that long wavelengths correspond to high threshold value in *a* and *c* directions. Therefore, different preparation conditions can be chosen to meet the requirements of transmittance in different wavelengths.

4.2.2 Reflection and Absorption of LDHs

The reflection and absorption of UV light are largely dependent on the layered structure of LDHs. The rigid LDH laminates could effectively reflect UV light, and multiple decrements of UV intensity may occur through multilayer reflection of UV light [34]. Moreover, the difference of metal elemental composition in LDHs layers may result in different performance of UV shielding. It was known that the UV-shielding properties of MgAl-LDH are highly related to the particle scattering and reflection of LDH layers. However, the replacement of Mg by Zn atom in the layer may further improve the UV-shielding properties [34, 40]. Figure 7a shows

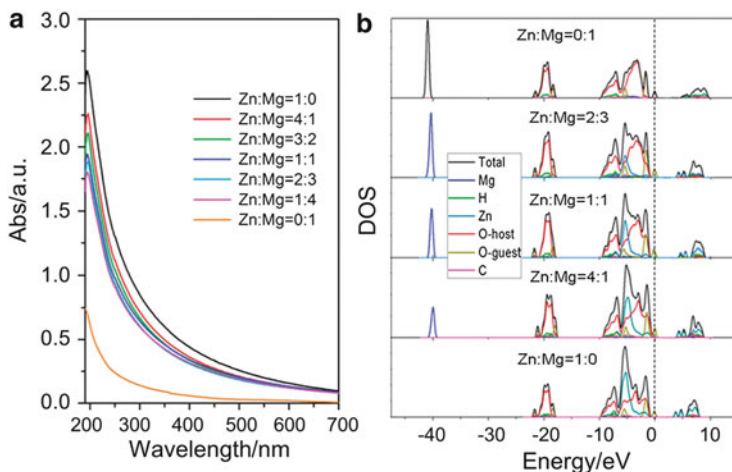


Fig. 7 (a) UV–Vis absorption spectra of the $((\text{Zn}_x\text{Mg}_y)_2\text{Al-CO}_3\text{-LDH/PAA})_{10}$ films ($x:y = 1:0, 4:1, 3:2, 1:1, 2:3, 1:4$ and $0:1; x+y = 1.0$); (b) the density of states for the $(\text{Zn}_x\text{Mg}_y)_2\text{Al-CO}_3\text{-LDHs}$ ($x:y = 0:1, 2:3, 1:1, 4:1$ and $1:0; x+y = 1.0$) [34]

the UV–Vis absorption spectra of the $((\text{Zn}_x\text{Mg}_y)_2\text{Al-CO}_3\text{-LDH/PAA})_{10}$ films which are assembled by polyacrylate (PAA, without any UV absorption) and LDHs with the same particle size but different $\text{Zn}^{2+}/\text{Mg}^{2+}$ ratios [34]. The results show that the UV absorption capacity enhances along with the increased $\text{Zn}^{2+}/\text{Mg}^{2+}$ ratios. The calculated density of states (DOS) of the $(\text{Zn}_x\text{Mg}_y)_2\text{Al-CO}_3\text{-LDHs}$ are shown in Fig. 7b, which indicates that the UV absorption of the pure $\text{Mg}_2\text{Al-CO}_3\text{-LDHs}$ is due to the interlayer CO_3^{2-} anions. Compared with the $\text{Mg}_2\text{Al-CO}_3\text{-LDHs}$ (4.58 eV), a decrease in the bandgap (3.33–4.16 eV) of the $(\text{Zn}_x\text{Mg}_y)_2\text{Al-CO}_3\text{-LDHs}$ occurs, which facilitates the increase in photon absorption efficiency. Therefore, the employment of Zn element is beneficial to tune the transition mode, electron structure, bandgap, and UV-shielding properties of LDH materials.

4.3 Host–Guest Interaction and UV-Shielding Performances

Due to the versatility and ions exchangeable properties of LDH materials, a number of anions with strong UV absorption properties have been intercalated into the interlayer of LDHs. Therefore, the UV-shielding properties of the LDH-based materials can be effectively improved due to the synthetic effects of interlayer absorption, particle scattering, and structural reflection in the layer. Moreover, the host–guest interaction between interlayer guests with LDHs layers may further influence their shielding properties.

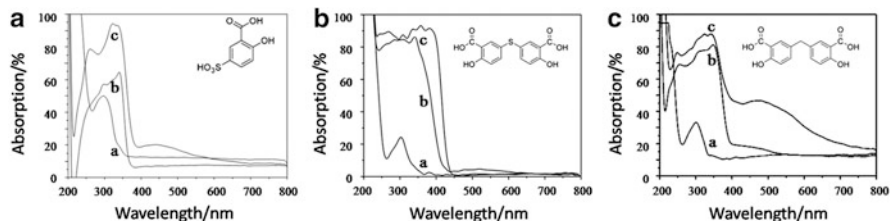


Fig. 8 UV absorption curves of (A) SSA-LDHs, (B) TDSA-LDHs, and (C) MDSA-LDHs composites, and the details are (a) ZnAl-NO₃-LDHs, (b) UV absorbents, and (c) intercalated LDHs, and the insets show the structures of UV absorbents [42–44]

4.3.1 Salicylic Acid and Esters

Salicylic acid and esters are commonly used as organic UV absorbents; Xing et al. [41] have prepared sodium salicylate (SS) intercalated LDHs by ion-exchange method. The obtained supramolecular materials exhibit advanced UV-shielding properties and promoted stability, which can be due to the electrostatic interaction and hydrogen bond between LDHs and guest ions. UV transmittance measurements indicate that the UV-shielding performance is highly improved for the ZnAl-SS-LDHs, compared with the pristine SS and ZnAl-CO₃-LDHs samples. In addition, some other salicylate compounds, including 5-sulfosalicylic acid (SSA) [42], 5, 5'-thiodisalicylic acid (TDSA) [43], and 5,5'-methylenedisalicylic acid (MDSA) [44], have been intercalated into LDHs, and the resulting LDHs composites exhibit promoted UV absorption performance (Fig. 8).

4.3.2 Benzophenones

He et al. [33] have prepared 2-hydroxy-4-methoxybenzophenone-5-sulfonic acid (HMBA, an organic UV absorbers) assembled Zn-Al-LDHs through ion-exchange method, and the obtained composites possess better UV absorption ability and high stability. Moreover, HMBA/LDH system can also be obtained by the SNAS method [45]. The intercalated LDHs composites had a strong UV absorption capacity, and a broad-range characteristic can be attributed to the regular arrangement of HMBA in LDHs galleries (Fig. 9A). Photostability tests were carried out by irradiating the samples under UV light for different time. The UV absorption intensity of pure HMBA has decreased for about 20 % in the 200–400 nm after UV irradiation accompanied by a significant increase in absorption in the visible region, which indicates a structural change for the HMBA (Fig. 9B). For the HMBA-LDHs composites, except for the slight change due to the degradation of absorbed HMBA on LDHs surface, there is almost no obvious change during the UV irradiation (Fig. 9C). Thus, significantly improved photostability was obtained upon the intercalation of UV absorbents.

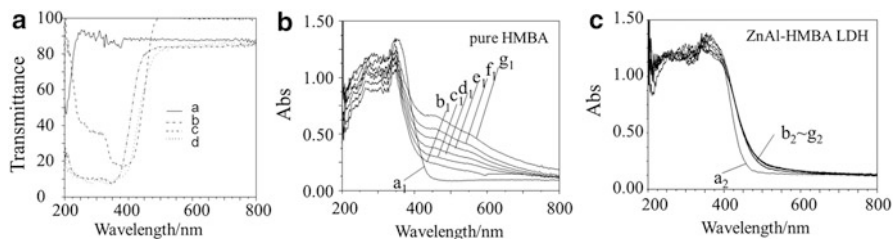


Fig. 9 (A) UV-Vis absorption curves of (a) ZnAl-CO₃-LDHs, (b) pure HMBA, (c) sodium HMBA, and (d) ZnAl-HMBA-LDHs; UV-Visible absorption curves of (B) pure HMBA and (C) ZnAl-HMBA-LDHs after different times of UV irradiation, (a)–(g): 0 min, 15 min, 30 min, 45 min, 60 min, 75 min, and 90 min [45]

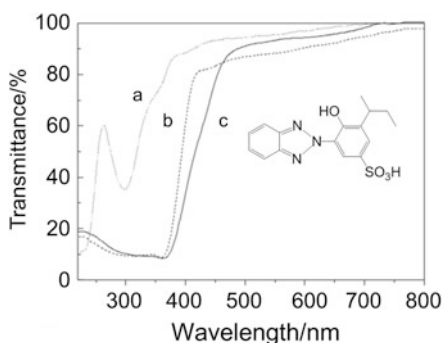


Fig. 10 UV transmittance curves of (a) ZnAl-NO₃-LDHs, (b) BZO, and (c) ZnAl-BZO-LDHs, and the inset shows the structure of BZO [46]

4.3.3 Benzotriazole

Tuo et al. [35, 46] have intercalated 5-benzotriazolyl-4-hydroxy-3-sec-butylbenzenesulfonic acid (BZO) into interlayer of LDHs by ion-exchange method using ZnAl-NO₃-LDHs as a precursor. Figure 10 shows the UV transmittance curves of intercalated BZO-LDHs composites as well as the pure LDH and BZO precursors. UV absorption bands of ZnAl-NO₃-LDHs are located around 300 and 230 nm (Fig. 10a), and BZO possesses strong absorption below 400 nm (Fig. 10b). After intercalation, the BZO/LDH exhibits a broader range of UV shielding compared with the pristine BZO (Fig. 10c) and also maintains high visible light transmittance.

4.3.4 Others

Some other organic UV absorbers have also been intercalated into the interlayer galleries of LDHs, and superior UV blocking properties, visible light transmittance,

Table 3 Molecules and its structure of UV absorbers for intercalation

Interlayer guest molecules	Structure	Refs.
4-Hydroxy-3-methoxybenzoic acid		[33]
4-Hydroxy-3-methoxycinnamic acid		[33]
4,4'-Diaminostilbene-2,2'-disulfonic acid		[33]
p-Aminobenzoic acid		[33]
Urocanic acid		[33]
Cinnamic acid		[47]
p-Methoxycinnamic acid		[47]
2-Phenylbenzimidazole-5-sulfonic acid		[35, 48]
3,6-Dihydroxynaphthalene-2,7-disulfonate		[36]
2-Naphthylamine-1,5-disulfonic acid		[36, 49]
2,3-Dihydroxynaphthalene-6-sulfonic acid		[36, 50]
Aurintricarboxylic acid		[51]

and photo- and thermal stability can also be obtained. The molecules and their chemical structures are listed in Table 3.

4.4 Application of LDH-Based UV-Shielding Materials in Polypropylene and Asphalt

4.4.1 Polypropylene

Polypropylene (PP) is one of the most common plastic, but its application has been hindered due to the weak photostability. The mechanical properties of PP are usually affected by the UV photo-oxidative degradation under sunlight [43, 44]. To improve the anti-UV ability of PP, photostabilizers with

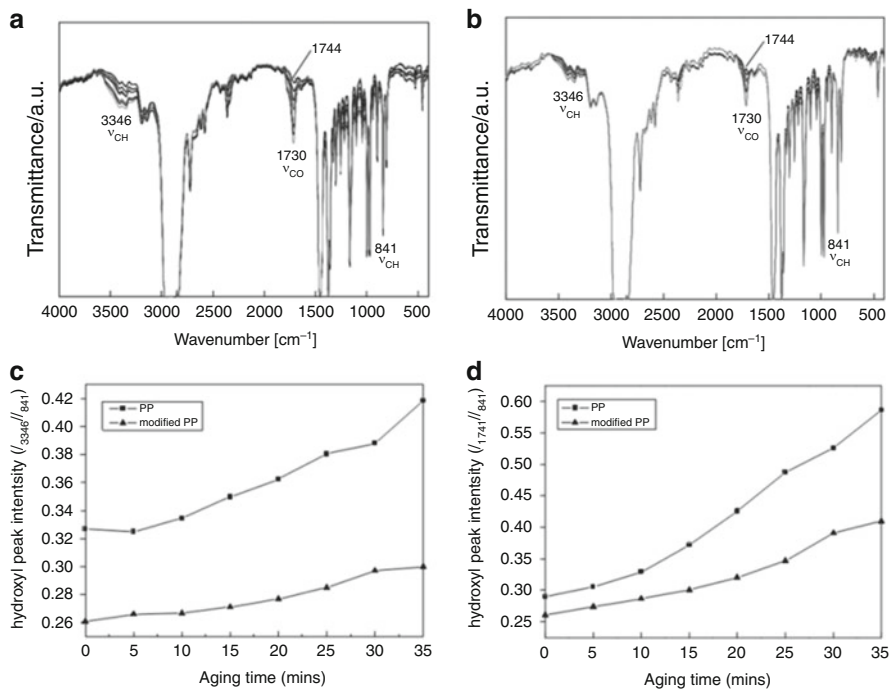


Fig. 11 FT-IR spectra of (a) pristine PP and (b) PP modified with 1% ZnAl-BZO-LDHs under UV irradiation for 35 min, and the relative peak intensities of (c) hydroxyl and (d) carbonyl bands for pristine PP and LDH-modified PP (1%) [35]

UV-shielding properties have been added to the PP composite [35, 42, 49–51]. Figure 11 shows the compared IR reflectance spectra of PP films with and without the addition of ZnAl-BZO-LDHs during photodegradation process [35]. Wavenumbers at 1,456, 1,376, 1,165, 974, 841, and 808 cm^{-1} are characteristic IR absorption bands of PP and ZnAl-BZO-LDHs/PP (Fig. 11a, b) samples. The absorption intensity ratios $I(\text{carbonyl})/I(\text{C-H})$ and $I(\text{hydroxyl})/I(\text{C-H})$ can be calculated (Fig. 11c, d), and the results show that the rate for formation of C=O and OH/OOH groups in ZnAl-BZO-LDHs/PP under UV irradiation is significantly lower than that in the pristine PP. Therefore, the addition of ZnAl-BZO-LDH has markedly blocked the UV light and prevented the degradation of PP and thus enhances the photostability. Figure 12 shows the digital photos of pristine PP and LDH-modified PP after UV exposure for 15 min. It was found that the pristine PP film becomes brittle after exposure to UV light, while the LDH-modified sample maintains high mechanical properties under the same conditions. This result further confirms that LDHs can effectively shield UV light to prevent degradation.

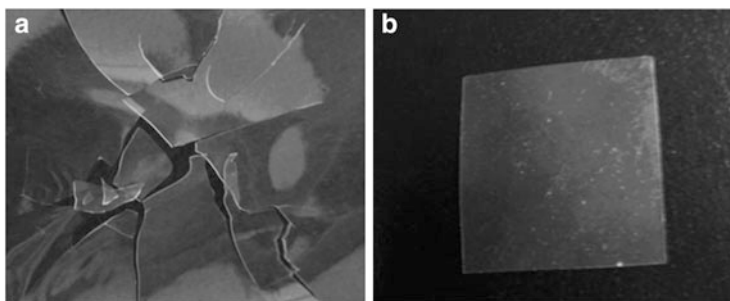


Fig. 12 Photographs of (a) pristine PP and (b) LDH-modified PP after UV exposure for 15 min [35]

Table 4 Softening point increment and VAI values for three asphalt samples [41]

Sample	Initial softening point (°C)	Softening point after 4 days (°C)	ΔS (°C)	Initial viscosity (Pa·s)	Viscosity after 4 days (Pa·s)	VAI
Pristine asphalt	49.3	55.4	6.1	0.926	1.137	0.228
Asphalt with 3 wt % $Mg_4Al_2CO_3$ -LDH	50.2	51.7	1.5	1.102	1.330	0.207
Asphalt with 3 wt % $Zn_4Al_2CO_3$ -LDH	49.2	50.4	1.2	1.064	1.254	0.179

4.4.2 Asphalt Pavement

As a highly viscous mixture of polycyclic aromatic hydrocarbon, asphalt has been widely used in road constructions. However, UV radiation always leads to the aging of asphalt, which is caused by the chemical transformation of the containing organic polymers. The aging of asphalt would subsequently affect the upper layers of the pavement, resulting in cracking, stripping, or other degradation of the pavement. Considering the serious damages of pavement, it is important to find new ways to improve the ability of asphalt to delay UV radiation.

In order to investigate the practical application, the law of solar radiation was studied, and a series of artificial tests (such as accelerated aging tests, rheological, and viscoelastic measurements) have been carried out. Important parameters in evaluating the aging resistance ability of asphalt, such as viscosity aging index (VAI) and softening point increment (ΔS) after aging, are obtained. The higher values of VAI and ΔS correspond to samples with weaker antiaging properties [52]. Wang et al. [40] have performed UV light irradiation tests of asphalt and composite of asphalt with 3 wt% LDHs in an accelerated weather tester for 4 days. Table 4 shows that the values of VAI and ΔS for the asphalt doped with LDHs are lower than those of the pristine asphalt, especially for VAI values. Digital photos in

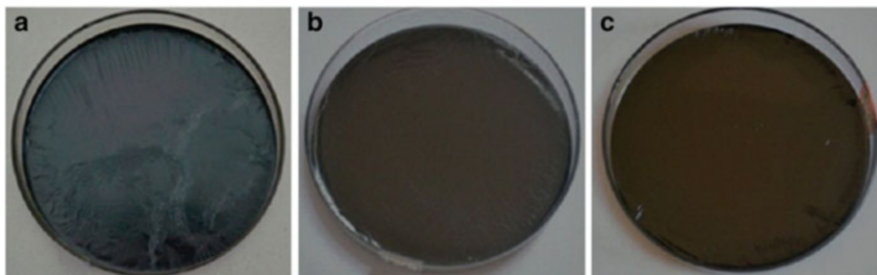


Fig. 13 Asphalt samples aged in UV light for 4 days: (a) pristine asphalt, (b) asphalt with 3 wt% MgAl-CO₃-LDH, and (c) asphalt with 3 wt% ZnAl-CO₃-LDH [41]

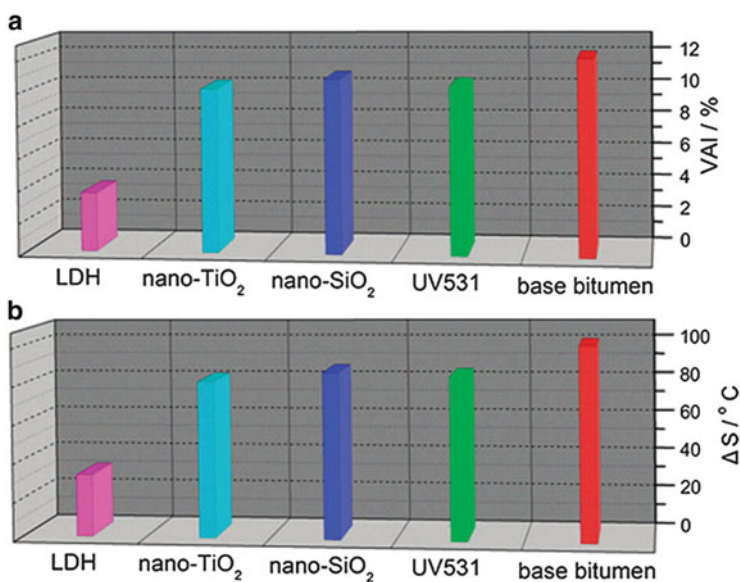


Fig. 14 (a) Viscosity aging index and (b) softening point increment of base bitumen and the four modified bitumen after irradiation with a UV lamp (500 W, 15,000 $\mu\text{W cm}^{-2}$) for 12 days [34]

Fig. 13 have further confirmed the enhanced antiaging performances of LDH-modified asphalt. Thus, it can be concluded that the employment of LDHs as anti-UV aging agents can result in enhanced photostability and prolonged service lifetime of asphalt. As well, Shi et al. [34] have investigated the UV resistance properties of LDHs. The values of VAI and ΔS show that the LDH-incorporated asphalt possesses superior performances than those modified by commercial UV absorbents (such as UV 531, SiO₂ and TiO₂), demonstrating a promising UV-resistance agent (Fig. 14).

5 LDH-Based IR Absorption Materials and the Application

5.1 Introduction of IR Absorption Materials

Solar light plays a crucial role in the photosynthesis and the growth of things on earth. However, the heat supplied by solar during the daytime would rapidly lose as heat radiation at night, which restricts the growth of plants to some extent. The heat loss from the earth surface to the surrounding is usually diffused by means of low-energy mid-infrared radiation, ranging from 7 to 25 μm ($1,428\text{--}400\text{ cm}^{-1}$) with the peak in the range of 9–11 μm ($1,111\text{--}909\text{ cm}^{-1}$). Therefore, to keep the temperature and prevent heat loss, agricultural plastic films (agri-film) [53, 54] are widely used in “green house.”

Polymers, such as low-density polyethylene (LDPE), are commonly used agri-films for crop harvest and energy saving [55, 56]. However, LDPE has poor heat preservation, and the heat is rapidly lost through the film at night [57]. To effectively enhance the ability of heat storage of agri-film, some additives are needed. The heat-preservation additives should block the loss of long-wavelength IR at night and maintain transmission of visible light during the daytime [55, 58]. Some inorganic additives, such as French chalk, china clay, and metal oxides (ZnO , TiO_2 , and Sb_2O_3), were incorporated as IR absorbents [54, 59, 60]. However, the contained impurities and variable particle sizes have accelerated the degradation of the film, and their transmittance of visible light and mechanical property are unsatisfactory [61]. Therefore, there is a need to develop materials with high purity and controllable particle size as alternative inorganic heat-preservation additives used in agri-films.

5.2 IR Absorption Properties of LDHs

LDHs have been used as IR absorption materials due to the uniform particle size, high crystallization degree, good photo-/thermal-stability, and tunable IR absorption abilities due to the changeable metal-oxide vibrations. By adding the LDHs particles into agri-film, the IR absorption ability, transparency, heat-preservation capacity, and the mechanical properties can be improved.

5.2.1 IR Absorption Ability

LDHs can strongly absorb IR due to the vibration of metal-oxide bonds in host layer and the interlayer anions [62]. For the typical CO_3^{2-} intercalated LDHs, the broad peak around $3,441\text{ cm}^{-1}$ can be ascribed to the stretching vibration of OH groups attached to the metal atoms in the LDH layers. The band at about $1,625\text{ cm}^{-1}$ can be

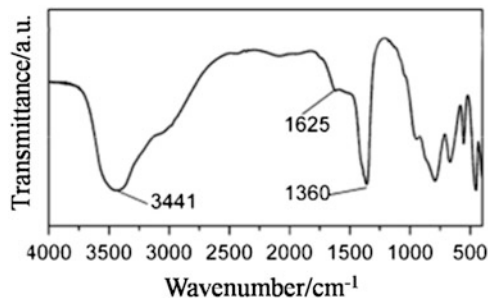


Fig. 15 FT-IR spectra of MgAl-CO₃-LDH [64]

Table 5 Typical heat-retention additives and their refractive index [67]

Materials	Refractive index	Materials	Refractive index
LDPE	1.51	MgAl-LDH	1.50
Silica	1.46	China clay	1.56
Light calcium carbonate	1.49	Diatomite	1.45
French chalk	1.55	Muscovite	1.58

attributed to the deformation vibration of water molecules in the interlayer domain. In addition to these absorption bands, characteristic peaks at 1,360, 840 and 671 cm⁻¹ can be attributed to the ν_3 vibration of CO₃²⁻ [63]. The vibrations of M-O units below 1,050 cm⁻¹ (Fig. 15) are the key characteristics for the applications in IR absorption materials [64]. Moreover, in order to extend the range of IR absorption, Eu-doped LDH was investigated [58, 65]. In addition to the common IR absorption, the employment of Eu resulted in broad vibration peaks in the range of 600–900 cm⁻¹ and 1,250–1,350 cm⁻¹, which has further improved the heat-preservation properties of agri-film.

5.2.2 Antireflection Property

The particle size of LDHs can be controlled due to different preparation methods [66]. Different from the traditional additives (such as the French chalk and china clay) with the particle size in the range of several μm , the LDH particles with the size distribution in the range of 50–500 nm can be obtained [64, 67]. Thus, LDHs with small size can be adopted as an alternative to promote dispersion degree in the agri-film. Moreover, the similar refractive index of LDHs and LDPE (illustrated in Table 5) has effectively reduced refraction phenomenon, leading to the low light loss and the promoted transparency in the agri-film.

5.2.3 Heat-Preservation, Photostability, and Antifogging Properties

To achieve high heat-preservation ability, visible light transparency and infrared irradiation blocking are significant. The LDH materials with high visible light transmittance enabled visible light get through the agri-film during the daytime, and the IR absorption properties of LDHs could prevent the infrared irradiation and heat loss at night.

As an additive, LDHs are highly stable under the photo-irradiation, which ensures their long service lifetime in practical use. Moreover, LDHs can absorb or isolate acidic groups and heavy metal ions to protect agri-film from degradation. Owing to the large specific surface area, porous structure, and oil absorption property of LDHs, the addition of LDHs enables controlled release of antifogging agent, which can further enhance the antifogging properties of agri-film.

However, the IR absorption of NO_3^- or CO_3^{2-} intercalated LDHs usually ranges from 7 to 8 μm , which cannot perfectly meet the strong IR loss at 9–11 μm (909–1,111 cm^{-1}). Therefore, the introduction of suitable anions with high IR absorption at 909–1,111 cm^{-1} is necessary to reduce the IR loss and further promote the capability of heat preservation of agri-film [68].

5.3 Intercalation and Performances of LDH-Based IR Absorption Materials

Several molecule-based systems possess strong IR absorption required for blocking heat irradiation. However, these molecules sometimes are acidic, and their direct use as additives may result in fast degradation or aging of the film. Therefore, the incorporation of these molecules (usually containing sulfate, carboxyl, and phosphate groups) into LDHs may be an effective way to achieve high photo- and thermal stability of the agri-film.

5.3.1 Intercalation with Inorganic Anions

Jiao et al. [63] have prepared $\text{Mg}_2\text{Al-CO}_3\text{-SO}_4\text{-LDH}$ via the ion-exchange method, and the obtained composites have well-defined crystal structure and present higher selective IR absorption ability than the pristine $\text{Mg}_2\text{Al-CO}_3\text{-LDHs}$. The peaks at 1,104 and 1,194 cm^{-1} can be attributed to the ν_3 vibration of SO_4^{2-} , associated with peaks at 1,019 and 619 cm^{-1} for ν_1 and ν_4 vibrations (Fig. 16). Therefore, the $\text{Mg}_2\text{Al-CO}_3\text{-SO}_4\text{-LDHs}$ possess better selective IR absorption properties.

Phosphate groups (such as the vibrations of P–O and P=O) present strong IR absorption in the range of 1,300–900 cm^{-1} which is exactly the region required for effective absorption of heat irradiation. Wang et al. [69, 70] have prepared phosphate groups intercalated MgAl-LDHs . As shown in Fig. 17, peaks at 1,253 cm^{-1}

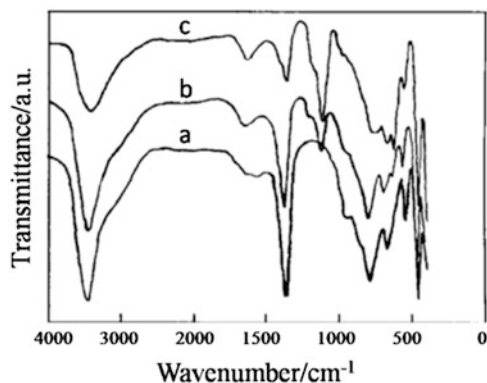


Fig. 16 IR spectra of samples exchanged by SO_4^{2-} for different time: (a) 0 h, (b) 4 h, and (c) 16 h [63]

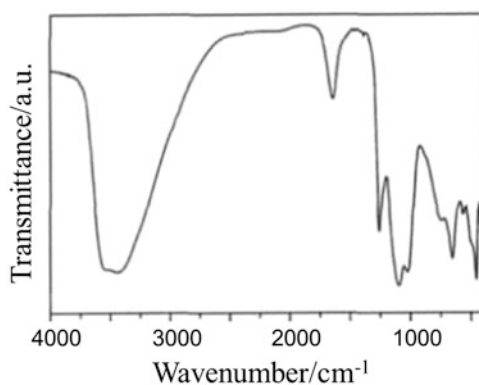


Fig. 17 IR spectra of $\text{MgAl-H}_2\text{PO}_4\text{-LDH}$ [69]

Table 6 Average transmittances of mixed $\text{MgAl-H}_2\text{PO}_4\text{-LDHs}$ and $\text{MgAl-CO}_3\text{-LDHs}$ in different ranges [69]

Sample	7–14 μm	7–25 μm	9–11 μm
$\text{MgAl-CO}_3\text{-LDHs}$	34.5	29.7	39.5
$\text{MgAl-CO}_3\text{-LDHs:MgAl-H}_2\text{PO}_4\text{-LDHs}$ (3:1)	28.9	26.3	37.2
$\text{MgAl-CO}_3\text{-LDHs:MgAl-H}_2\text{PO}_4\text{-LDHs}$ (2:1)	27.1	25.2	24.6
$\text{MgAl-CO}_3\text{-LDHs:MgAl-H}_2\text{PO}_4\text{-LDHs}$ (1:1)	23.6	21.5	19.8
$\text{MgAl-CO}_3\text{-LDHs:MgAl-H}_2\text{PO}_4\text{-LDHs}$ (1:2)	25.0	22.6	18.5
$\text{MgAl-CO}_3\text{-LDHs:MgAl-H}_2\text{PO}_4\text{-LDHs}$ (1:3)	25.6	23.2	18.3
$\text{MgAl-H}_2\text{PO}_4\text{-LDHs}$	28.2	24.2	17.8

and $1,091\text{ cm}^{-1}$ are attributed to the vibration of PO_2 , while the peak at $1,020\text{ cm}^{-1}$ is due to the stretching vibration of P-OH . Further experiment was carried out by mixing $\text{MgAl-CO}_3\text{-LDH}$ and $\text{MgAl-H}_2\text{PO}_4\text{-LDH}$ at different ratios (Table 6), and

employment of H_2PO_4 has effectively improved the selective IR properties compared with pristine $\text{MgAl-CO}_3\text{-LDH}$, especially in the region of 9–11 μm . In order to fabricate materials with comprehensive IR absorption properties, all of the IR regions (such as 7–25, 7–14 and 9–11 μm) should be taken into consideration. The sample with the ratio of $\text{MgAl-CO}_3\text{-LDH}$ and $\text{MgAl-H}_2\text{PO}_4\text{-LDH}$ at 1:1 possess optimized absorption ability in these three region. As another example, Badreddine et al. [71] have prepared a series of phosphate anions (such as PO_3^- , H_2PO_4^- , HPO_4^{2-} , PO_4^{3-} , $\text{P}_2\text{O}_7^{4-}$ and $\text{P}_3\text{O}_{10}^{5-}$) intercalated LDH composites, and the obtained composites displayed largely promoted IR absorption properties.

5.3.2 Intercalation with Organic Anions

Some organic anions containing phosphate groups have also been intercalated into the interlayer of LDHs [70], and the LDH-based composites with different IR absorption intensity and selectivity were obtained. For example, Wang et al. have employed *N,N*-Bis(phosphonomethyl)glycine (GLYP) [53], aminotrimethylene-phosphonic acid (ATMP) [55], and *N*-phosphonomethyliminodiacetic acid (PMIDA) [59, 62] as interlayer guests (Fig. 18) to promote the IR absorption capacity in the range of 909–1,111 cm^{-1} in the composites. Thus, the obtained hybrid materials possess higher infrared absorption than the original $\text{MgAl-CO}_3\text{-LDH}$, and the heat loss via the radiation to the atmosphere environment can be effectively inhibited.

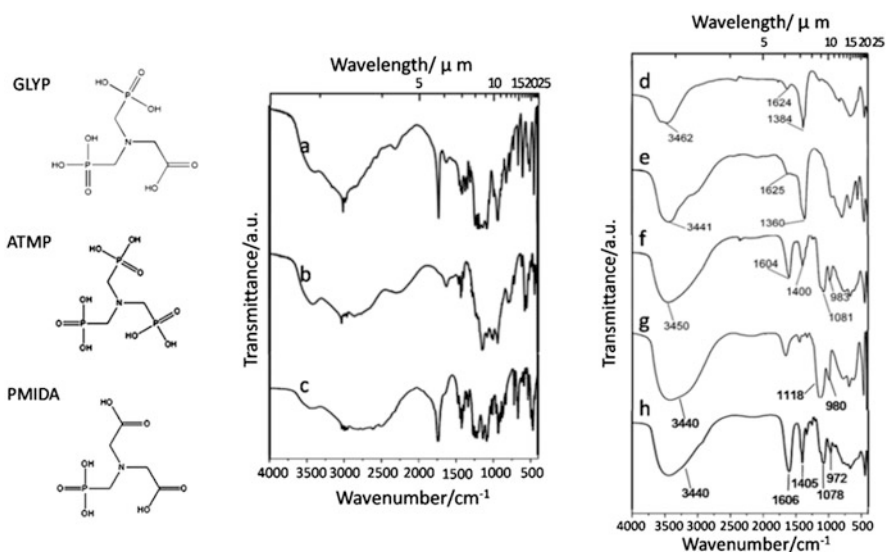


Fig. 18 Molecular structure and IR spectra of (a) GLYP, (b) ATMP, (c) PMIDA, (d) $\text{MgAl-NO}_3\text{-LDH}$, (e) $\text{MgAl-CO}_3\text{-LDH}$, (f) MgAl-GLYP-LDH , (g) MgAl-ATMP-LDH , and (h) MgAl-PMIDA-LDH [53, 55, 59]

5.4 Application of LDH-Based IR Absorption Materials

The obtained MgAl-X-LDHs, X = H_2PO_4^- [69], GLYP [53], ATMP [55], PMIDA [59], and IDA [62]) were mixed with LDPE to form the LDH/LDPE composite films by the master batch technology [67, 72]. Taking the MgAl-GLYP-LDH as an example [53, 70], TEM images of LDH/LDPE composites (4 wt% loadings of GLYP-LDH and CO_3 -LDH) are shown in Fig. 19. The continuous gray areas stand for the polymer matrices, while the dark dots in left pictures represent LDHs composites. It can be clearly seen that both GLYP-LDH and CO_3 -LDH particles are uniformly dispersed in the polymer matrices without any aggregation of clusters.

The TG-DTA curves of LDPE, GLYP-LDH/LDPE, and CO_3 -LDH/LDPE are shown in Fig. 20. The DTA curves in three samples show endothermic transition at about 130 °C (melting point of LDPE). The main weight loss is between 270 and 500 °C with an exothermic peak at 410 °C which can be attributed to the degradation of the hydrocarbon chains [73–75]. However, for GLYP-LDH/LDPE and CO_3 -LDH/LDPE, the weight loss begins at 320 °C and 380 °C, respectively, and the exothermic peaks shift to 420 °C and 425 °C. Moreover, the T_{50} values (the temperature corresponding to 50 % weight loss) for LDPE, GLYP-LDH/LDPE, and CO_3 -LDH/LDPE are calculated at 420 °C, 460 °C, and 450 °C, respectively. Therefore, it can be concluded that addition of LDHs composites has effectively promoted the thermal stability of LDPE film.

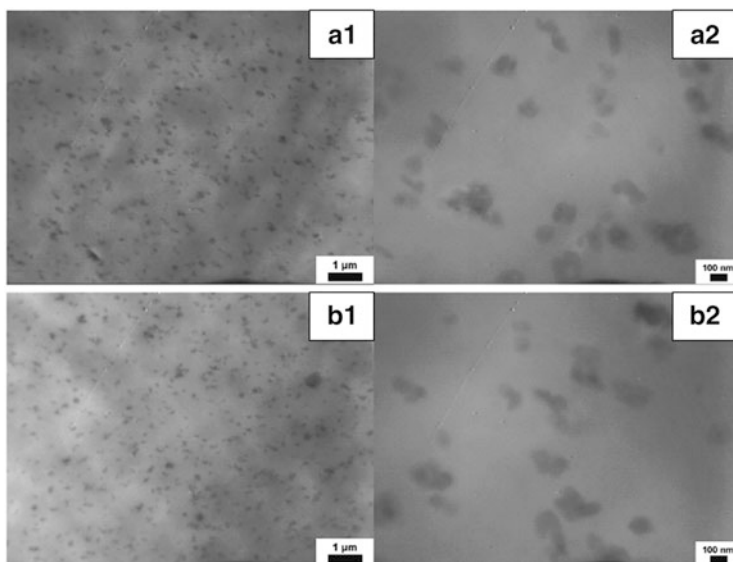


Fig. 19 TEM images of LDH/LDPE composites with 4 wt% loadings of (a) GLYP-LDH and (b) CO_3 -LDH at different magnification scales (scale bar: 1 μm for left and 100 nm for right pictures) [53]

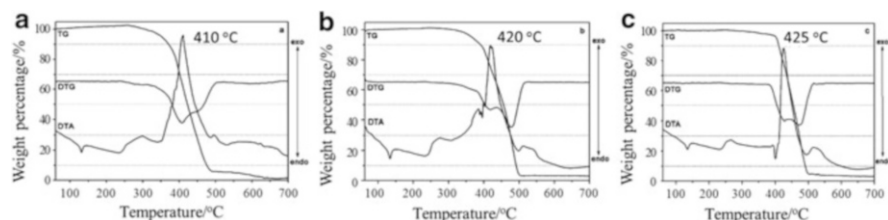


Fig. 20 TG-DTA-DTG curves of (a) LDPE, LDH/LDPE composites with 4 wt% loadings of (b) GLYP-LDH and (c) CO_3 -LDH [73, 74]

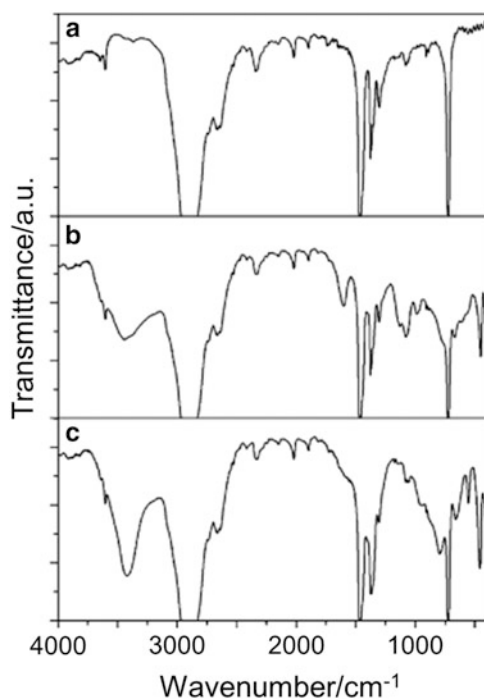


Fig. 21 FT-IR spectra of (a) pure LDPE film and LDH/LDPE films with 4 wt% loadings of (b) GLYP-LDH and (c) CO_3 -LDH [73, 74]

Figure 21 shows the FT-IR spectra of the LDPE film, GLYP-LDH/LDPE, and CO_3 -LDH/LDPE film. Compared with the pristine LDPE film, the CO_3 -LDH-doped LDPE composite exhibits superior infrared radiation in the range of $1,428\text{--}400\text{ cm}^{-1}$, while GLYP-LDH/LDPE displays advanced infrared absorbing ability in the range of $909\text{--}1,111\text{ cm}^{-1}$. In addition, mechanical properties of incorporated LDPE films were also carried out, and the average values of breaking elongation and tensile strength are shown in Table 7. Compared with LDPE film, the breaking elongation property was promoted after the addition of LDHs, and the tensile strength was just slightly reduced. Therefore, the addition of LDHs would not influence the mechanical properties of LDPE.

Table 7 Mechanical properties of LDPE and LDH/LDPE [73, 74]

Samples	Breaking elongation (%)	Tensile strength (MPa)
LDPE	442.3	14.0
MgAl-GLYP-LDH/LDPE	447.2	13.3
MgAl-CO ₃ -LDH/LDPE	447.1	13.6

6 Fabrication and Application of LDH-Based Host–Guest Luminescent Materials

The photoactive guest molecules assembled into the LDHs host layers can achieve new type of host–guest composite materials with advanced photo-related performances (such as luminescence). There are several advantages for the accommodation of photofunctional species into LDHs inorganic matrices:

1. LDHs layers can provide a confined and isolated microenvironment for the intercalated guest molecules. In the confined interlayer space, the vibration and thermal motion of guests could be inhibited, and this may effectively improve the luminescent efficiency of the photoactive molecules. Furthermore, the photofunctional guests with different emission can be assembled into the host layers in a step-by-step manner, in which the rigid LDH layers can avoid the permeation between different guest molecules.
2. The regular and crystalline LDHs layers allow the ordered arrangement and high orientation of interlayer guest molecules based on host–guest interactions. By tuning the chemical composition and charge density of host layers as well as the amount, arrangement and aggregation state of the guest molecules, the photo-related performance can be finely adjusted.
3. Due to the introduction of LDHs layers, the thermal- and photostability of the intercalated composites can be largely improved. Thus, the problem involving the stability of pristine organic materials in the practical applications can be resolved effectively.
4. The combination of transparent insulating LDHs layers with photoactive molecules may form an inorganic/organic multi-quantum-well structure. The insulating LDHs can act as energy barrier layers in the quantum well, which can accelerate the formation of exciton and improve the fluorescence efficiency.
5. Based on the changes in the aggregation states and/or the conformations of the interlayer photoactive molecules induced by the external environmental stimuli, the corresponding photo-related properties can be further tuned due to the alternations of host–guest and guest–guest interactions. Therefore, the LDH-based intelligent-responsive materials can be further constructed.

According to the design strategies mentioned above, a number of host–guest photofunctional materials have been continuously reported. In the following section, we mainly focus on the host–guest photofunctional materials with tunable static and dynamic luminescence.

6.1 *The Basic Guest Units of LDH-Based Photofunctional Materials*

To date, both the organic and inorganic photoactive species (including polymers, complexes, small molecules, quantum dots, and polyoxometalates) can serve as good candidates as guest molecules to assemble with LDHs. And the difficulties, such as the aggregation-induced quenching, lifetime and stability are eager to be solved. Table 8 gives typical examples of the interlayer photofunctional guests and their related fabrication methods.

6.2 *Fabrication of LDH-Based Photofunctional Material*

6.2.1 Layer-by-Layer Assembly

Layer-by-layer (LbL) assembly is a widely used method to achieve multilayer LDH-based ultrathin films (UTFs), which involves alternative dipping a substrate in positively charged LDH nanosheets and negative-charged photofunctional molecules [129]. Based on their electrostatic interactions, the guest molecules can be accommodated into the interlayer of LDH nanosheets. The employment of LDH nanosheets has provided an opportunity to finely tune the arrangement and relative distance of the interlayer molecules, and the homogeneous distribution of photofunctional molecules can be obtained [130]. Due to the confined and ordered environment provided by the rigid LDHs nanosheets, the luminescence quenching commonly caused by the aggregation and/or accumulation of photoactive molecules can be efficiently reduced. Moreover, the existence of inorganic layers may improve the thermal and optical stability of the photofunctional molecules [76]. Therefore, LbL assembly has supplied an effective way for the fabrication of hybrid UTFs with advanced photo-related properties.

Assembly Based on π -Conjugated Polymers

Luminescent organic polymer materials have attracted extensive attention, particularly due to their applications in optoelectronic devices, such as liquid-crystal displays [131, 132]. However, the development of these polymers is severely hindered by their short lifetime and poor photo- or thermal stability [133]. Yan et al. have presented a potential solution to these problems by assembling the polymers with rigid LDH nanosheets which can serve as a new inorganic/organic quantum well structure. Several anionic polymers, such as the derivatives of poly(p-phenylene) [76], poly(phenylenevinylene) [78], and polythiophene [79], have been studied, and investigation on a sulfonated poly(p-phenylene) anionic derivate (APPP) will be particularly introduced below.

Table 8 Photofunctional guests used in LDH-based composites and their fabrication methods

Materials	Categories	Molecules	Method	Refs.
Organic	Polymers	Poly(p-phenylene) anionic derivate (APPP)	LbL	[76, 77]
		Poly(5-methoxy-2-(3-sulfopropoxy)-1,4-phenylene-vinylene anionic derivate (APPV)	LbL	[77, 78]
		Sulfonated polythiophene (SPT)	LbL	[79, 80]
		Polydiacetylene (PDA)	LbL	[81]
		Poly{1-4[4-(3-carboxy-4-hydroxyphenylazo)benzenesulfonamido]-1,2-ethanediyl sodium salt} (PAZO)	LbL	[82]
	Complexes	Tris(1,10-phenanthroline-4,7-diphenyl-sulfonate)ruthenium (II) ([Ru(dpds) ₃] ⁴⁺)	LbL	[80, 83]
		Bis(8-hydroxyquinolate)zinc, tris(8-hydroxyquinolate-5-sulfonate) aluminum	LbL/co-intercalation	[84–87]
		[Tetrakis(4-carboxyphenyl)-porphyrinato]zinc(II) (ZnTPPC)	Ion exchange	[88]
		Pd(II)-5,10,15,20-tetrakis(4-carboxyphenyl) porphyrin (PdTPPC)	Coprecipitation	[89]
		5,10,15,20-Tetrakis(4-sulfonatophenyl) porphyrin (TPPS) and its palladium complex (PdTPPS)	Coprecipitation	[89–91]
		Zinc phthalocyanines (ZnPc)	Coprecipitation	[92]
		Tris[2-(4,6-difluorophenyl)pyridinato-C ² ,N]iridium(III) (Ir(F ₂ ppy) ₃)	LbL	[93]
	Small molecules	Sulforhodamine B (SRB)	Co-intercalation	[94]
		Bis(<i>N</i> -methyl-acridinium) (BNMA)	LbL	[77, 95]
		3,4,9,10-Perylene tetracarboxylate (PTCB)	LbL/co-intercalation	[96, 97]
		Benzocarbazole (BCZC)	Coprecipitation	[98]
		Bis(2-sulfonatostyryl)biphenyl (BSB)	LbL	[99]
		Sulfonated derivate of cyanin (Scy)	LbL	[100]
		2,2'-(1,2-Ethenediyl)bis[5-[[4-(diethylamino)-6-[(2,5-disulfophenyl) amino]-1,3,5-triazin-2-yl]amino] benzene-sulfonic acid] hexasodium salt (BTBS)	LbL	[101, 102]

(continued)

Table 8 (continued)

Materials	Categories	Molecules	Method	Refs.
		4,4'-Bis[2-di(b-hydroxyethyl) amino-4-(4-sulfophenylamino)-s-triazin-6-ylamino] stilbine-2,20-disulfonate (BBU)	LbL	[103]
		α -Naphthalene acetate (α -NAA) and β -naphthalene acetate (β -NAA)	Ions exchange	[104, 105]
		Fluorescein	Co-intercalation	[106, 107]
		2,2'-Azino-bis(3-ethylbenzothiazoline-6-sulfonate) (ABTS)	LbL	[108]
		Calcein	LbL	[109]
		Coumarin-3-carboxylate (C3C)	Coprecipitation	[110]
		(2,2'-(1,2-Ethenediyl)bis [5-[[4-(diethylamino)-6-[(2,5disulfophenyl) amino]-1,3,5-triazin-2-yl] amino]benzene sulfonate anion (BTZB)	Coprecipitation	[111]
		4-(4-Anilinophenylazo) benzenesulfonate (AO5)	Co-intercalation	[112]
		1,3,6,8-Pyrenetetrasulfonat acid tetrasodium salt (PTS)	LbL	[113]
		9-Fluorenone-2,7-dicarboxylate (FDC)	Co-intercalation	[114]
		2-Phenylbenzimidazole-5-sulfonate (PBS)	Co-intercalation	[115]
Inorganic	Quantum dots	CdTe	LbL	[102, 116–121]
		CdSe/ZnS	LbL	[118]
		InP/ZnS	Coprecipitation	[122]
		CdSe/CdS/ZnS	LbL	[123]
		CdS	Ions exchange	[124]
		ZnS	Ions exchange	[125]
	Polyoxometalates	$\text{Na}_9[\text{EuW}_{10}\text{O}_{36}]\cdot 32\text{H}_2\text{O}$ (EuW_{10})	LbL	[126, 127]
		$[\text{EuW}_{10}\text{O}_{36}]^{9-}$, $[\text{Eu}(\text{BW}_{11}\text{O}_{39})_2(\text{H}_2\text{O})_3]^{6-}$ and $[\text{Eu}(\text{PW}_{11}\text{O}_{39})_2]^{11-}$	Ions exchange	[128]

The LbL assembly process of the (APPP/LDH) $_n$ UTFs was monitored by UV–Vis absorption spectroscopy (Fig. 22), in which the absorption intensity at about 207 nm and 344 nm attributed to $^1\text{E}_{1u}$ and π – π^* transition of phenylene increases linearly along with the bilayer number n (Fig. 22a, inset), indicating a stepwise and uniform deposition procedure. Figure 22b shows the fluorescence emission spectra of (APPP/LDH) $_n$ UTFs, and the sharp peak at 415 nm shows a monotonic increase, consistent with the increase of bilayer number of (APPP/LDH) unit. The gradual

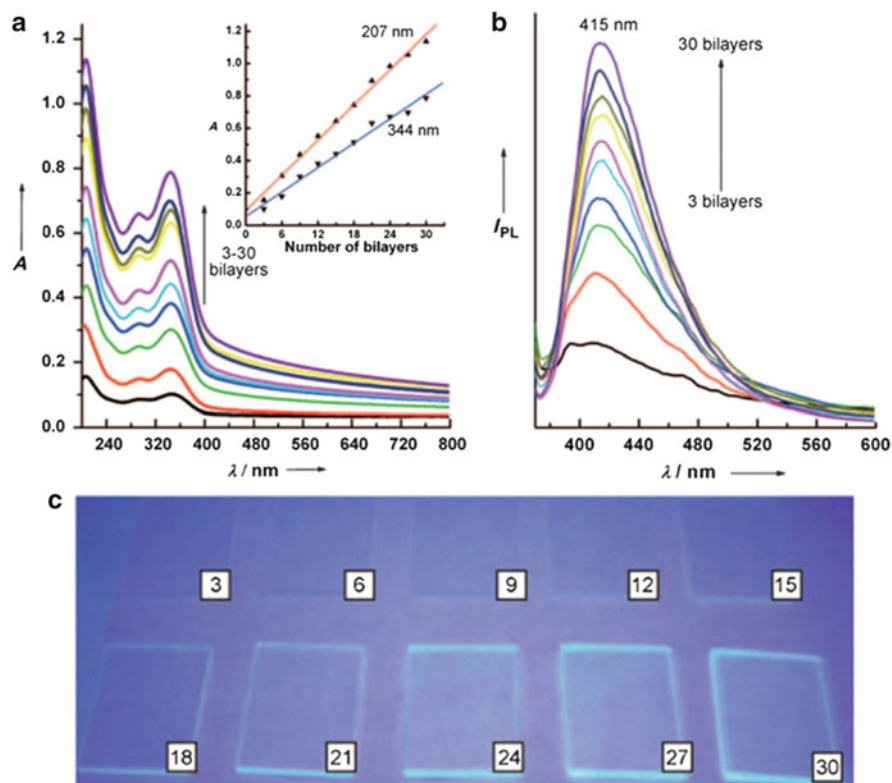


Fig. 22 Characterizations of $(\text{APPP/LDH})_n$ ($n=3-30$) UTFs: (a) UV-Vis absorption spectra (inset shows the linear correction of absorbance at 207 and 344 nm vs. n), (b) fluorescence spectra, and (c) photographs under 365 nm UV irradiation at different values of n [76]

change in luminescence can also be seen from photographs under UV light (Fig. 22c). Moreover, the UTFs with different n show no obvious shift or broaden in the absorption and fluorescence emission spectra, and this phenomenon suggests that no aggregation of APPP was formed during the assembly process.

The top-view SEM image (Fig. 23a) displays the homogeneity and uniformity of $(\text{APPP/LDH})_9$ UTFs. Thickness of 20–23 nm for $(\text{APPP/LDH})_9$ UTF was obtained from the side-view SEM image (Fig. 23b), with the average value about 2.5–2.8 nm for the basic unit of $(\text{APPP/LDH})_1$. The AFM topographical image ($3 \mu\text{m} \times 3 \mu\text{m}$) is illustrated in Fig. 23c with the root-mean-square roughness of 5.8 nm, indicating a smooth surface. Figure 23d shows the homogeneous distribution of the APPP chromophore throughout the film as dark blue color under the fluorescence microscope.

The fluorescence lifetime of $(\text{APPP/LDH})_n$ UTF (18.63–21.05 ns) is largely prolonged compared with the pristine APPP solution (0.88 ns). This remarkable increase is a result of isolation of the adjacent polymer provided by rigid LDH

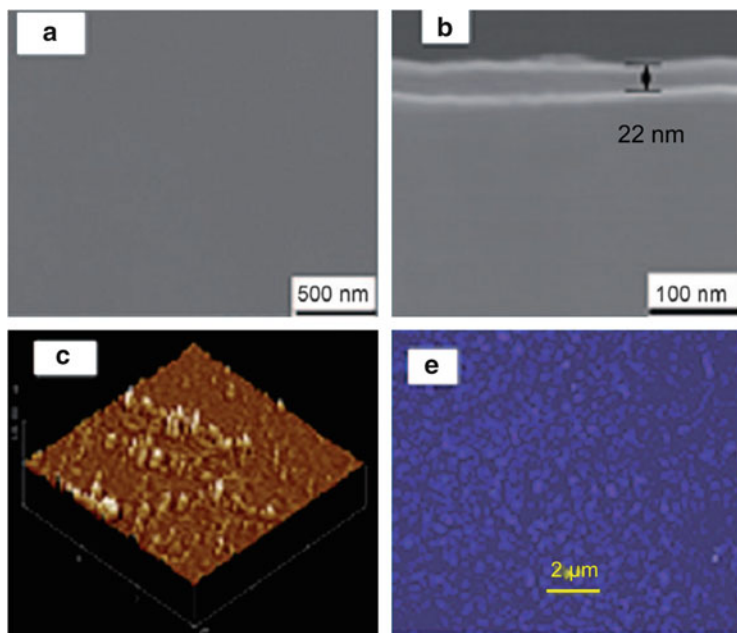


Fig. 23 The morphology of (APPP/LDH)₉ UTF: (a) top view of SEM image, (b) side view of SEM image, (c) tapping-mode AFM image, and (d) fluorescence microscope image [76]

nanosheets. Moreover, APPP molecules are confined within the interlayer environment of the LDH, and the inhibited thermal vibration of the APPP backbones may also contribute to the prolonged lifetime.

Photostability of (APPP/LDH)₂₇ UTF was performed under UV irradiation, and (APPP/PDDA)₂₇ (PDDA, polydimethylallylammonium chloride) was tested as a reference sample. As seen in Fig. 24, ~70 % of initial fluorescence intensity of (APPP/LDH)₂₇ UTF remained after continuous irradiation for 2 min, in contrast to ~50 % for (APPP/PDDA)₂₇ with the same measurement. Broadened emission band was observed for (APPP/PDDA)₂₇ UTF after 15 min, while no obvious band shift was found for (APPP/LDH)₂₇ in the whole test. It can be concluded that (APPP/LDH)₂₇ UTF possesses better UV light resistance ability compared with (APPP/PDDA)₂₇.

Assembly Based on Anionic Metal Complexes and Small Molecules

Transition-metal-based photoactive complexes have been extensively investigated in optoelectronics due to their high chemical stability and excellent luminescence properties [134]. Ruthenium-based complexes, tris(1,10-phenanthroline-4,7-diphenylsulfonate)ruthenium(II) (denoted as Ru(dpds)₃), have been studied by

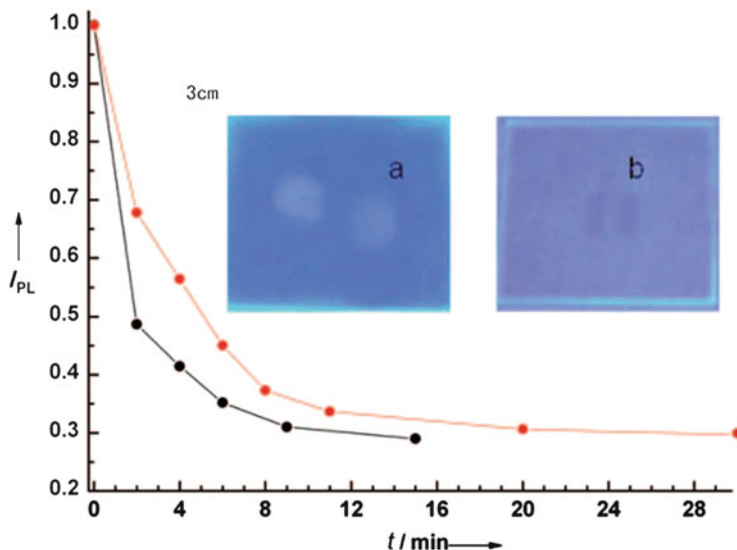


Fig. 24 Decay of normalized maximal PL intensity with time, normalized against the initial PL value; $\lambda_{\text{ex}} = 365$ nm to probe the UV irradiation resistance ability of (APPP/PDDA)₂₇ (black data points) and (APPP/LDH)₂₇ UTF (red) irradiated under 344 nm UV light. Insets: photographs under UV light of (a) (APPP/PDDA)₂₇ and (b) (APPP/LDH)₂₇ UTFs after the UV resistance experiment was finished [76]

assembly with LDH nanosheet to obtain orderly UTFs [83]. Figure 25 has illustrated the assembly process of (Ru(dpds)₃/LDH)_n UTFs, and UV-Vis absorption and fluorescence emission spectra have been employed to monitor the process with the increased intensity when varying the number of bilayers. Except for the periodic long-range ordered structures, well-defined red photoluminescence for the UTFs, the ordered Ru(dpds)₃ has overcome symmetry due to interaction with LDHs, and polarized photoluminescence behavior was observed. Other small molecules such as sulfonated carbocyanine derivate (Scy) [100] can also be directly assembled with LDH nanosheet, and the fluorescence performance and stability can be largely improved for the assembled UTFs.

Assembly Based on Positive-Charged and Low-Charged Molecules

Due to the charge-balance rule, it has been known that only anionic species can be directly assembled into the galleries of the positively charged LDH layers. This largely restricts the development of LDH-based functional materials, and the assembly of LDH nanosheets with abundant functional cations remains a challenge. To meet this requirement, Yan et al. [95] have proposed a new assembly strategy for cation-LDH UTFs by employing a suitable polyanion as the carrier. Bis(*N*-methylacridinium) (BNMA, an important dye in the field of chemiluminescence)

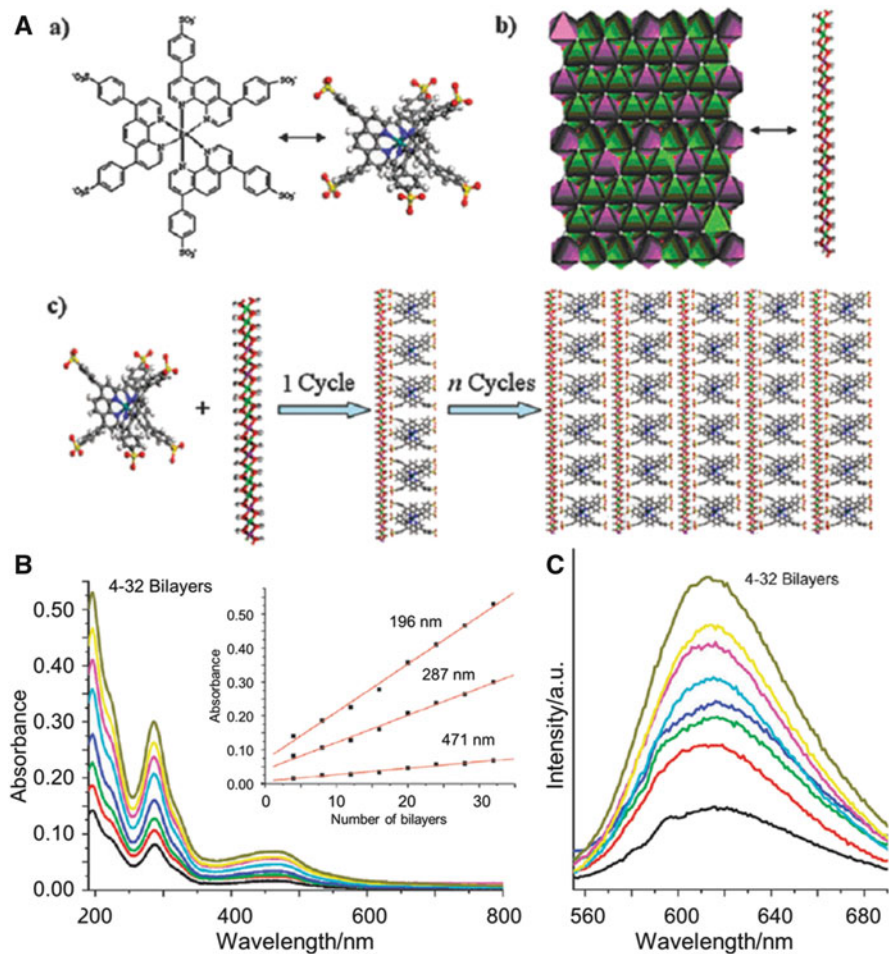


Fig. 25 (A) Schematic representation of assembly process of $(\text{Ru}(\text{dpds})_3/\text{LDH})_n$: (a) structure of $[\text{Ru}(\text{dpds})_3]^{4-}$, (b) representation of a monolayer of MgAl-LDH (dark pink, $\text{Al}(\text{OH})_6$ octahedra; green, $\text{Mg}(\text{OH})_6$ octahedra), and (c) assembly process; (B) UV-Visible absorption spectra (inset shows plots of the absorbance at 196, 287 and 471 nm vs. n), and (C) fluorescence emission spectra [83]

and an optically inert polyanion polyvinylsulfinate (PVS) was taken as examples for fabrication of $(\text{BNMA}@\text{PVS}/\text{LDH})_n$ UTFs, and the co-assembly process involves two steps. Firstly, BNMA is mixed with the main chain of the PVS, based on Coulombic interaction at the molecular level, and a cation–polyanion pair (BNMA@PVS) with negative charge and functional behavior of BNMA can be obtained. Subsequently, this negatively charged (BNMA@PVS) pair was assembled with LDH nanosheet via LbL process, whereby the cations and polyanion were stably coexisted in the gallery environment provided by LDH nanosheets.

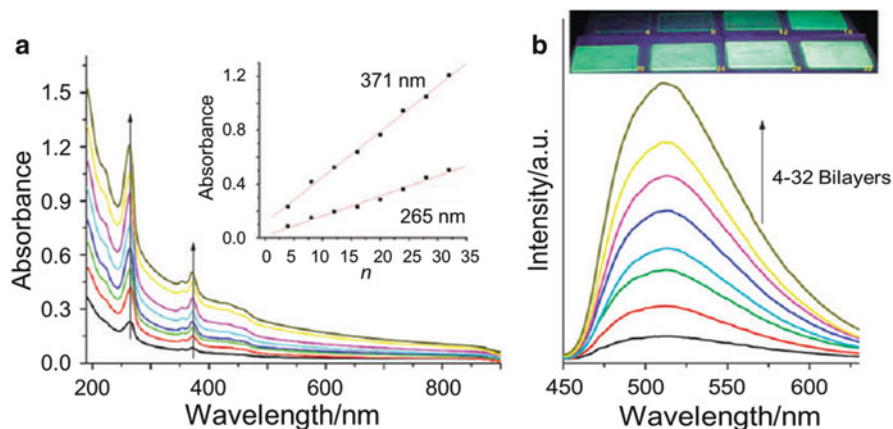


Fig. 26 (a) UV-Vis absorption spectra, (b) fluorescence spectra of the $(\text{BNMA@PVS/LDH})_n$ ($n=4-32$) UTFs. The insets in (a) and (b) show the plots of absorbance at 265 and 371 nm vs. n and optical photographs under 365 nm UV irradiation, respectively [95]

UV-visible absorption spectra were measured to monitor the assembly process for $(\text{BNMA@PVS/LDH})_n$ UTFs. The linearly increased intensities at 265 and 371 nm which correspond to the characteristic absorption bands of BNMA demonstrated an ordered and regular film growth procedure (Fig. 26a). Fluorescence emission intensity at 510 nm also presents consistent enhancement with the increase of bilayer number n (Fig. 26b), which can be confirmed by increased luminescence brightness under UV light irradiation (the inset of Fig. 26b). These results demonstrated successful co-assembly of BNMA@PVS pairs into the interlayer of LDHs. Moreover, the absorption and fluorescence emission spectra show no obvious red or blue shift compared with the pristine BNMA solution, suggesting uniform distribution throughout the whole assembly processing.

Top-view SEM (Fig. 27a), AFM (Fig. 27c) and fluorescence microscopy (Fig. 27d) images show that the assembled UTFs exhibit a homogeneous and continuous surface, indicating that the BNMA chromophores are distributed uniformly throughout the whole film. Side-view SEM image (Fig. 27b) reveals an approximate 1.5 nm for per $(\text{BNMA@PVS/LDH})_1$ bilayer, in accordance with the basal spacing obtained by XRD. This result further confirms a uniform and periodic layered structure of the multilayer film.

The molecular dynamic (MD) simulation was carried out to further understand the geometric structures of this new type UTF system. An idealized BNMA@PVS/LDH structural model was constructed, and the computational basal spacing is ca. 1.47 nm, in agreement with the experimental results. The simulation shows that the organic ions are found to adopt an ordered arrangement with a preferred orientation (15° between N-N axis to layers) in the as-prepared UTF, and the driving force for the UTF assembly is mainly dominated by the Coulomb interaction.

Moreover, several small low-charged molecules or molecules with poor assembled force can also be co-assembled into interlayer of LDHs by employing

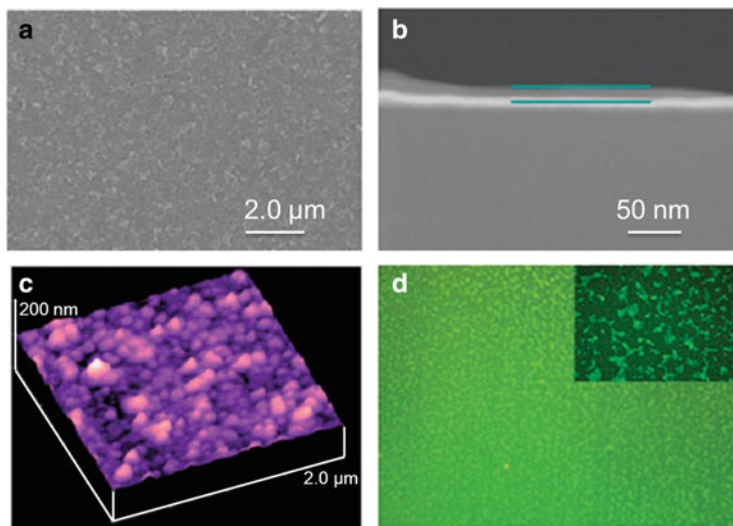
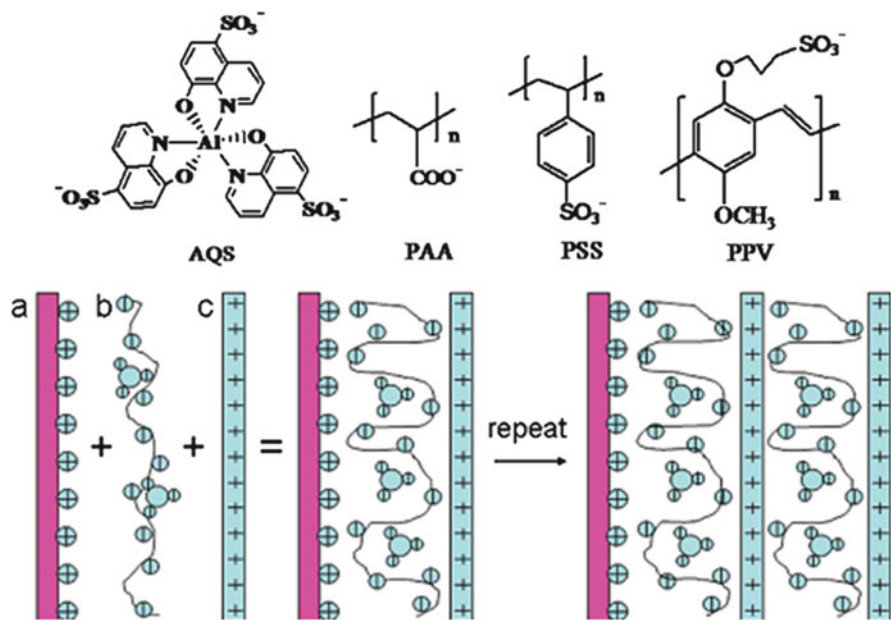


Fig. 27 The morphology of $(\text{BNMA@PVS/LDH})_8$ UTF for (a) top-view SEM image, (b) side-view SEM image, (c) tapping-mode AFM image, and (d) fluorescence microscope image multiplied by 50-fold and 1,000-fold (the inset plot) [95]

polyanions. For example, Li et al. [84] have achieved the co-assembly of the tris(8-hydroxyquinolate-5-sulfonate) aluminum (AQS^{3-}) with three polyanions [polyanions poly(acrylic acid) (PAA), poly(styrene 4-sulfonate) (PSS), and poly[5-methoxy-2-(3-sulfopropoxy)-1,4-phenylene vinylene] (PPV)] to obtain the hybrid UTFs, denoted as $(\text{AQS@PAA/LDH})_n$, $(\text{AQS@PSS/LDH})_n$, and $(\text{AQS@PPV/LDH})_n$ (Scheme 2). And similar work was also carried out by employing PSS and PVS to co-assemble with PTCB (perylene 3,4,9,10-tetracarboxylate) [97]. Therefore, the small complex anion–polyanion is anticipated to enhance the cohesion to assemble with LDH for UTFs. The luminous properties of such ordered UTFs can also be modulated by alternating the polyanion species and proportion.

Assembly Based on Electroneutral Molecules

A micellar assembly route for combination of neutral molecules and LDH nanosheets has been put forward in the absence of interaction between them. For example, neutral bis(8-hydroxyquinolate)zinc (Znq_2) can be encapsulated into the block copolymer poly(tert-butyl acrylate-co-ethyl acrylate-co-methacrylic acid) (PTBEM) micelles, and then the anionic block copolymer micelles $\text{Znq}_2\text{@PTBEM}$ were assembled with the exfoliated LDH nanosheets to obtain hybrid $(\text{Znq}_2\text{@PTBEM/LDH})_n$ UTFs (Fig. 28a) [87]. The as-prepared UTFs present a stepwise growth by varying number of bilayers, which can be observed in fluorescence emission spectra and corresponding photos under UV light (Fig. 28b).



Scheme 2 Schematic representation of the process for the fabrication of (AQS@polyanion/LDH)_n [84]

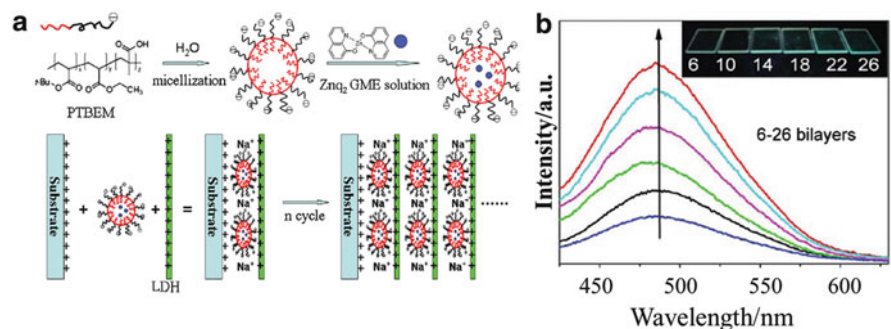


Fig. 28 (a) Schematic representation of the PTBEM, Znq₂, and MgAl-LDH nanosheet and the process for the fabrication of Znq₂@PTBEM micelle and (Znq₂@PTBEM/LDH)_n film; (b) photoemission spectra of (Znq₂@PTBEM/LDH)_n UTFs (*n* = 6–26) with the insets showing the photograph of UTFs under the 365 nm UV illumination [87]

Similar methods also appear for the neutral small molecules perylene [135] and tris [2-(4,6-difluorophenyl)pyridinato-C²,N]iridium(III) (Ir(F₂ppy)₃) [93]. With poly (*N*-vinyl carbazole) (PVK) as the carrier, (PVK@perylene/LDH)_n and (Ir(F₂ppy)₃@PVK/LDH)_n UTFs can be obtained based on hydrogen-bond LbL assembly. The obtained UTFs exhibit decent brightness and reversible two-state switching of the fluorescence emission with external organic compounds.

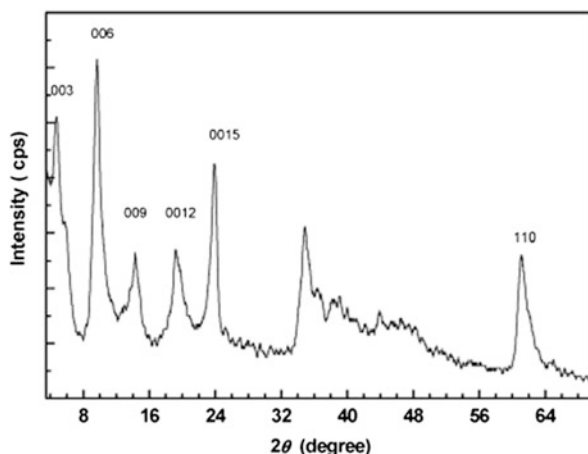
6.2.2 Intercalation Assembly

Intercalation is one of the most common methods to incorporate the photoactive molecules into the interlayer of LDHs, and the powdered forms of layered organic–inorganic composites can be obtained. Various anionic molecules can be intercalated due to the diversity of the composition in layers and ion exchangeable properties of LDHs. Several intercalation methods have been applied and developed, such as direct intercalation (typical coprecipitation), ions exchange, and co-intercalation. The intercalation of chromophore molecules into LDHs may efficiently inhibit the quenching problems induced by molecular aggregation, and the corresponding fluorescence properties can be largely improved.

Direct Intercalation

By the use of coprecipitation method, the single-component chromophore molecules can be intercalated into the LDH galleries. As an example, 3,4,9,10-perylene tetracarboxylate (PTCB) anion has been intercalated into LDH layers by dropwisely adding the mixed solution of sodium hydroxide and PTCB to the solution containing magnesium nitrate and aluminium nitrate [96]. Figure 29 shows the XRD pattern of as-prepared PTCB/LDH composites, the main characteristic reflections appeared at 4.771° (003), 9.641° (006), and 14.331° (009) indicated the successful intercalation of PTCB molecules. Good multiple relationships can be observed for d_{003} , d_{006} , and d_{009} between the basal, second- and third-order reflections. The stronger reflection of 006 compared with 003 implied that PTCB molecules are located in the symmetric center of the half-way plane within the interlayer region. The photophysical properties, thermolysis behavior, and orientation arrangements of the PTCB/LDH have been studied to compare with the pure PTCB. It was found that the intercalation into LDH has weakened the

Fig. 29 Powder XRD pattern of PTCB/LDH [96]



strong π - π interaction between PTCB anions, which has paved a way for solid-state optoelectronic devices with high performance.

Ion Exchange

The ion-exchange method is often employed as an alternative of direct intercalation, particularly if the guest anions are unstable in aqueous solution with the divalent or trivalent metal cations. According to the different stability and affinity of the interlayer guests, nitrate-LDH is always applied as a precursor in the ion-exchange process. For example, Shi et al. [104] have fabricated α -naphthalene acetate (α -NAA) and β -naphthalene acetate (β -NAA) intercalated LDH materials through ion-exchange method. The XRD in Fig. 30 show the successful intercalation of these two compounds. The basal spacing of $\text{Zn}_2\text{Al-NO}_3\text{-LDH}$ (Fig. 30a) powder is 0.87 nm, while 2.80 and 1.94 nm of basal spacing can be obtained when NO_3^- is replaced by α -NAA and β -NAA (Fig. 30b, c).

UV-Vis absorption spectra were used to investigate the status and arrangement of NAA in the interlayer of LDH. The pristine NAA in solution, physical mixture of NAA and LDH, and NAA intercalated LDH samples were measured. For the mixture of α -NAA and LDH, a broadened and red-shifted absorption band can be observed. The broaden of band is due to the existence of a continuous set of vibrational sublevels in each electronic state; red shift of 14 nm is the result of ordered and dense packing of molecules in the interlayer, and this may cause intermolecular interactions between NAA (Fig. 31A, line b). In contrast, the α -NAA intercalated LDH sample (curve c in Fig. 31A) exhibits a monomer form in the LDH galleries without any shift caused by intermolecular interactions. Similar results can be obtained for β -NAA samples (Fig. 31B). Moreover, other inorganic species (such as quantum dots [124, 125] and polyoxometalates (POMs) [128] can also be assembled into LDH through ion-exchange process, and the host-guest interaction can effectively affect the fluorescence properties of the guest molecules.

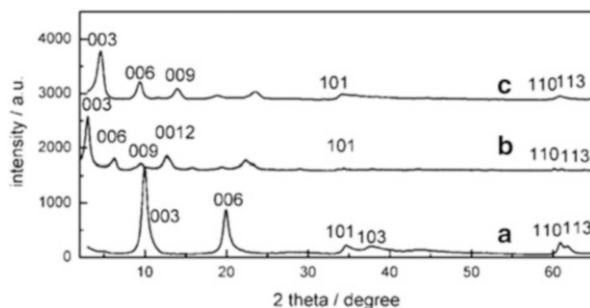


Fig. 30 XRD patterns for (a) $\text{Zn}_2\text{Al-NO}_3\text{-LDH}$ powder, (b) α -NAA-LDH powder, and (c) β -NAA-LDH powder [104]

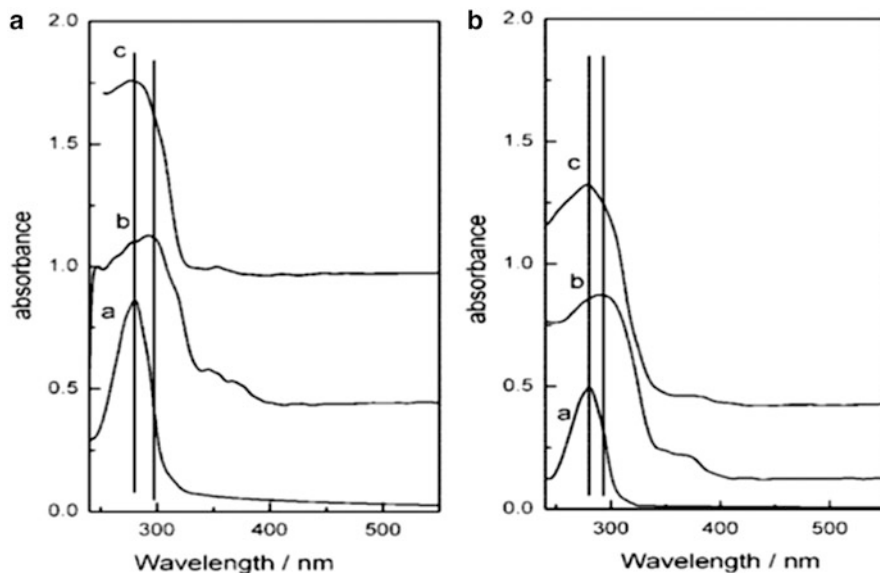


Fig. 31 UV-Vis absorption spectra of (A) α -NAA for (a) in solution, (b) mixed with LDH, and (c) intercalated in LDH; (B) β -NAA for (a) in solution, (b) mixed with LDH, and (c) intercalated in LDH [104]

Co-intercalation

Co-intercalation is an effective way if guest molecules are difficult to accommodate in the LDH layers. Frequently, surfactant, such as dodecyl sulfonate (DDS^-), 1-heptanesulfonic acid sodium (HES), and dodecylbenzene sulfonate (DBS) can be employed as the co-intercalation agents. The introduction of surfactant has provided an enlarged interlayer spacing, which facilitates the successful incorporation of guest. Moreover, a nonpolar and homogeneous microenvironment can be obtained due to surfactant, and thus, the adjustment of the orientation and aggregation status of photofunctional molecules can be achieved. The adjustment of ratio of fluorophore and surfactant within the LDH layer can effectively influence the fluorescence properties of guest molecules. Several fluorophores have been co-intercalated in the LDH layers, such as sulforhodamine B (SRB) [94], zinc phthalocyanines (ZnPc) [92], fluorescein (FLU) [106, 107, 136], ammonium 1-anilinonaphthalene-8-sulfonate (ANS) [137], and other similar systems (as shown in Table 8). The quantity of intercalated guest can be modulated through tuning the ratio of guest and surfactant, and the detailed information will be further introduced in Sect. 6.3.1.

6.3 Adjusting Photofunctionalities of LDH-Based Materials

6.3.1 Static Adjustment

Modulation Based on the Charge Density and Elemental Composition of Host Layer

By controlling the synthesis condition and mole ratio of raw materials, the charge density of the LDH layer can be varied in a wide range, which enabled the tunable photo-related properties of intercalated guest molecules. Luminescent benzocarbazole anions (BCZC), which possesses high quantum yield and good color purity, has been incorporated into LDH via coprecipitation with different layered charge densities of LDHs [98]. MgAl-LDHs with the Mg/Al ratio at 2 and 3.5 were employed to adjust the arrangement of the BCZC. Figure 32A shows the structural model for LDHs with different charge density. LDHs with host layer containing 12 Mg atoms and 6 Al atoms (Mg/Al ratio of 2, Fig. 32A-a) and 14 Mg atoms and 4 Al atoms (Mg/Al ratio of 3.5, Fig. 32A-b) have been adopted. The main characteristic peaks for BCZC/LDH samples present a good multiple relationship for the basal, second- and third-order reflections, with the basal spacing of 2.31 nm for Mg/Al ratio of 2 and 2.39 nm for Mg/Al ratio of 3.5 (Fig. 32B).

UV-Vis spectra of the pristine BCZC and intercalated BCZC have been studied. The absorption bands at 265, 289, and 320 nm can be attributed to the characteristic absorptions of carbazole-type dyes for BCZC in solution, while the solid sample of pristine BCZC and BCZC intercalated LDH composites possess a broadband at 295 and 410 nm due to the molecule stacking (Fig. 33A). Figure 33B shows the fluorescence emission spectra for these samples, and emissions in the range of 490–520 nm are displayed. It can be observed that the spectra of pristine BCZC in solution is similar with BCZC intercalated LDH with Mg/Al ratio at 2, while photoemission of the interlayer BCZC (Mg/Al ratio at 3.5) is close to that of its solid state. Therefore, it can be concluded that variation on the layered charge

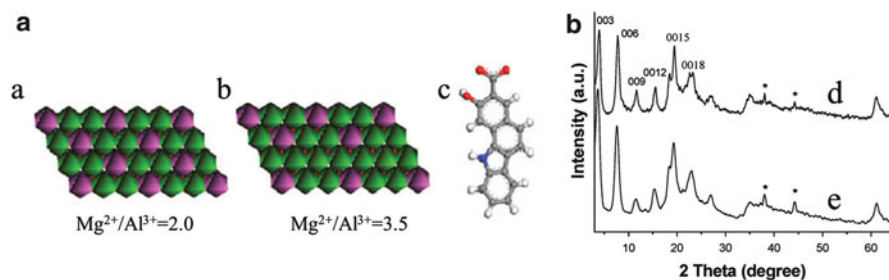


Fig. 32 (A) Structure model for the superlattice layer model for MgAl-LDH (dark pink: Al(OH)₆ octahedra; green: Mg(OH)₆ octahedra) for Mg/Al ratio of (a) 2 and (b) 3.5, and (c) structural model of BCZC; (B) XRD patterns of BCZC/MgAl-LDH (d, e stand for samples with Mg/Al ratio of 2 and 3.5, respectively; Asterisk: the Al substrate) [98]

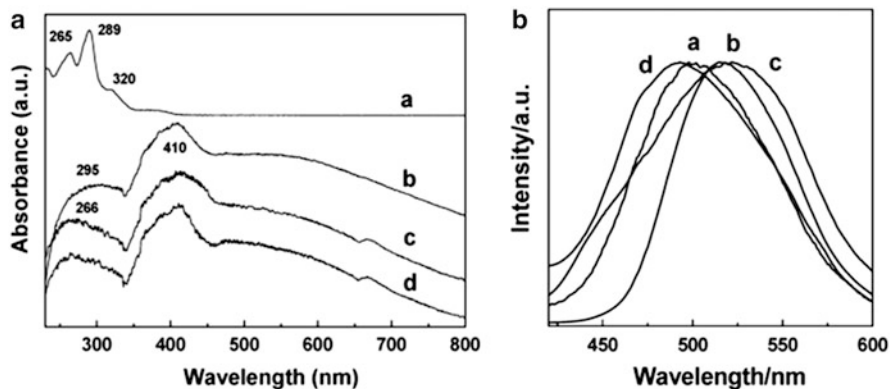


Fig. 33 (A) The UV-Vis absorption spectra and (B) normalized photoemission spectra for (a) pristine BCZC aqueous solution (10 mM), (b) solid BCZC, and BCZC/MgAl-LDH with the Mg/Al ratio of (c) 2 and (d) 3.5 [98]

density could effectively modify the luminescence performance of the guest dye molecules.

The chemical composition in the LDHs layer also serves as a parameter in modulating the luminescent behavior. For a sulfonated derivative of stilbene intercalated LDHs system [138], compared with the pure sample with the maximum emission wavelength ($\lambda_{\text{max}}^{\text{em}}$) located at 463 nm, the intercalation products exhibit tunable $\lambda_{\text{max}}^{\text{em}}$ in the range from 456 nm (Co₂Al-LDH as the layer) to 484 nm (Mg₂Al-LDH as the layer), demonstrating that the fluorescent wavelength can be continuously tuned by changing the chemical composition of LDHs, as a result of different host-guest interactions between the host layer and the interlayer anions.

Modulation Based on the Quantity of Interlayer Molecules

The orientation and aggregation state of interlayer guest can be tuned by controlling the contents of the interlayer chromophores, and thus, the fluorescence performance can also be varied. For example, rhodamine is a widely used fluorescent dye due to its high quantum yields, but its fluorescence properties are severely affected by its concentration, and a high concentration usually leads to aggregation and subsequent quenching [139]. Yan et al. have achieved the co-intercalation of sulforhodamine B (SRB) and dodecylbenzene sulfonate (DBS) with different ratios into LDHs [94]. Figure 34A shows the XRD pattern of SRB-DBS/LDH with different interlayer concentration of SRB, and it was observed that when the ration of intercalated SRB increased from 0 to 16.67 %, the spacing increased from 28.87 Å to the maximum 30.96 Å (Fig. 34A, curve a-g). And the spacing value has a decreasing trend when the quantity of SRB increased from 16.67 % to the maximum 100 % (Fig. 34A, curve h-k). This variation of the interlayer spacing may be a result of changeable distribution and arrangement of interlayered SRB with different ratios.

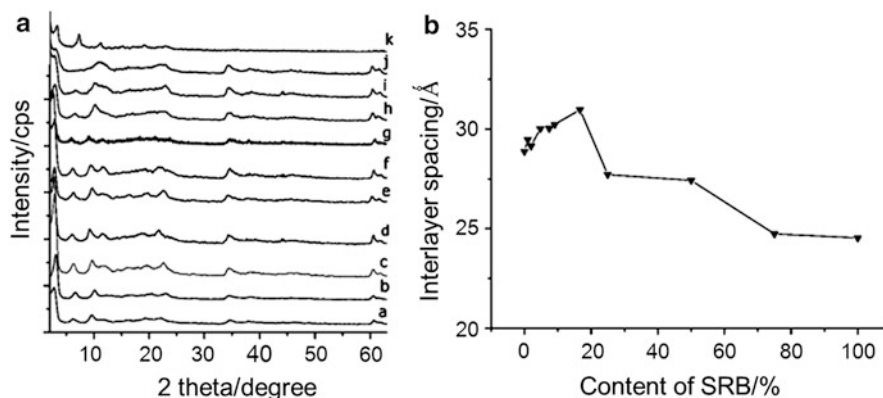


Fig. 34 (A) Powder XRD patterns of SRB(*x*%)-DBS/LDH (a, 0 %; b, 0.99 %; c, 1.96 %; d, 4.76 %; e, 7.41 %; f, 9.09 %; g, 16.67 %; h, 25.0 %; i, 50.0 %; j, 75.0 %; k, 100 %). (B) The plot of interlayer spacing vs. SRB concentration [94]

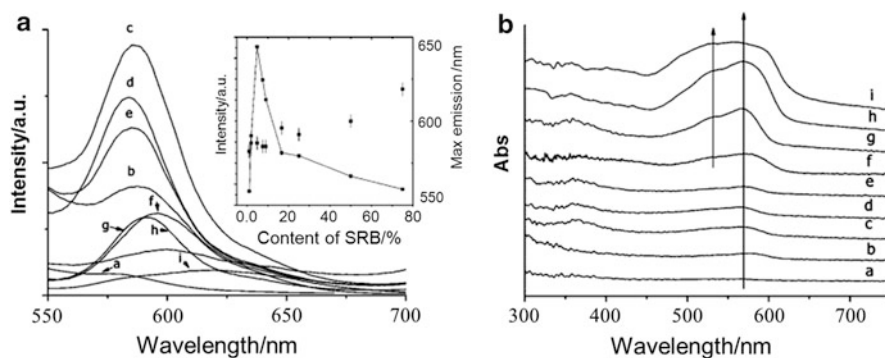


Fig. 35 Study of SRB(*x*%)-DBS/LDH with different SRB content: (a) 0.99 %, (b) 1.96 %, (c) 4.76 %, (d) 7.41 %, (e) 9.09 %, (f) 16.67 %, (g) 25.0 %, (h) 50.0 %, and (i) 75.0 % for (A) photoemission spectra (with the excitation wavelength of 360 nm and the inset shows the fluorescence intensity and the variation of maximum emission wavelength) and (B) solid UV-Vis absorption spectra [94]

The fluorescence emission behavior of SRB-DBS/LDHs with different SRB content has been studied, and the emission spectra are displayed in Fig. 35A. With the increase of SRB in SRB-DBS/LDHs, the intensity of fluorescence emission exhibits an increase to maximum (content of SRB is 4.76 %), followed by a continuous decrease. The emission peak varies from 587 to 619 nm as the SRB content increased to 75 %. This can be attributed to the variation of distribution status and arrangement of interlayer SRB, and high concentration may facilitate the formation of dye aggregation, accounting for the red shift and quenching in fluorescence emission. UV-Vis spectra (Fig. 35B) show that absorption peaks at

Table 9 The maximum wavelength of absorption and emission of the ZQS(*x*%)–DDS/LDH [86]

Sample	λ_{abs} (nm)	λ_{em} (nm)	PLQY (%)
DDS-ZQS(2 %)/Mg ₂ Al-LDH	258, 379	464	5.0
DDS-ZQS(5 %)/Mg ₂ Al-LDH	258, 381	479	24.4
DDS-ZQS(10 %)/Mg ₂ Al-LDH	256, 390	486	18.1
DDS-ZQS(20 %)/Mg ₂ Al-LDH	256, 395	487	17.3
DDS-ZQS(40 %)/Mg ₂ Al-LDH	256, 399	488	16.4
DDS-ZQS(60 %)/Mg ₂ Al-LDH	256, 396	491	9.6
DDS-ZQS(80 %)/Mg ₂ Al-LDH	256, 389	495	5.8
ZQS(100 %)/Mg ₂ Al-LDH	256, 385	497	2.3
DDS-ZQS(5 %)/Mg ₃ Al-LDH	258, 382	490	9.7
DDS-ZQS(5 %)/Zn ₂ Al-LDH	258, 377	491	27.4
DDS-ZQS(5 %)/Zn ₃ Al-LDH	258, 373	491	25.9
H ₂ ZQS crystal	258, 396	466	20.4
ZQS solution (5×10^{-5} mol L ⁻¹)	254, 368	516	–

360 and 570 nm increase as more SRB molecules were intercalated. An absorption shoulder at ca. 530 nm appears (SRB content of 16.67 %), indicating a formation of H-type aggregates.

For the fluorescence lifetime, compared with pristine SRB solution (2.38 ns), the fluorescence lifetime of SRB-DBS/LDH firstly increases with SRB content changed from 0.99 to 16.7 %, and the lifetime decreases when the content increased to 25 % (Table 9). The change in lifetime further indicates the aggregates of SRB, which is in accordance with emission and absorption spectra. Therefore, the absorption/emission intensity, wavelength, and fluorescence lifetime could be changed due to the variation of interlayer content.

As another example, Li et al. have prepared co-intercalated systems based on bis(8-hydroxyquinolate-5-sulfonate)zinc anion (ZQS²⁻) and DDS, and the fluorescence properties can also be changed obviously through adjustment of intercalation content [86]. Table 9 shows the fluorescence emission information of ZQS-DDS/LDHs. For different ratio of ZQS in the interlayer and different host layer composition, the maximum emission wavelength and quantum yields can be finely controlled. Furthermore, the brightest luminous intensity, together with the longest fluorescence lifetime, was observed for DDS-ZQS (5 %)/Mg₂Al-LDH.

Liang et al. have investigated the dispersion and corresponding singlet oxygen production efficiency of zinc phthalocyanines (ZnPc) after intercalation [92]. XRD patterns showed the basal spacing varied in the range of 23.6–24.6 Å with the content of ZnPc changed from 1 to 10 %, and the co-intercalation of ZnPc and SDS can be further demonstrated by FT-IR spectra. Compared with the pristine form of ZnPc in water and ethanol, the monomer dispersed state with maximum absorption at 678 nm can be obtained via intercalation into the LDH galleries (Fig. 36A, curve c), indicating a low polarity microenvironment provided by LDH gallery for the formation of monomeric ZnPc. With the ZnPc content increased from 1 to 10 %, the absorption intensity exhibit a gradual increase at 678 nm, while a broad absorption

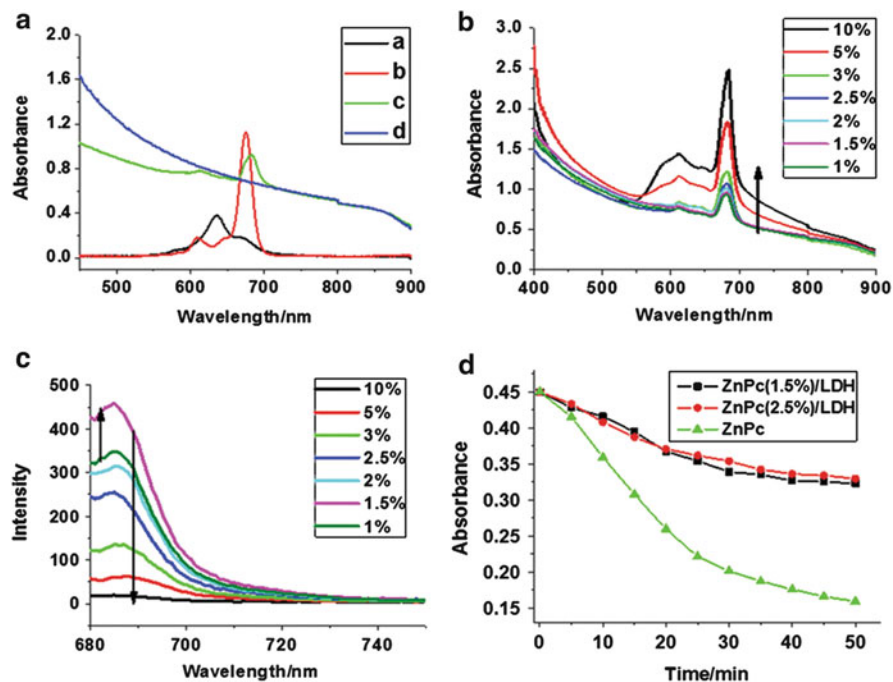


Fig. 36 (A) The UV–Vis absorption spectra: (a) pristine ZnPc (2×10^{-5} M) in aqueous solution, (b) pristine ZnPc (2×10^{-5} M) in 60 % ethanol solution, (c) ZnPc (1.5 %)/LDH (3×10^{-4} M) aqueous suspension, (d) pristine LDH (3×10^{-4} M) aqueous suspension. (B) The UV–Vis absorption spectra and (C) photoluminescence spectra of various ZnPc ($x\%$)/LDH suspension (3×10^{-4} M) with x ranging in 1–10 %. (D) Decay curves of absorption at 678 nm for ZnPc (1.5 %)/LDH, ZnPc (2.5 %)/LDH, and 635 nm for pristine ZnPc, respectively, as a function of irradiation time (650 nm) [92]

band appeared in 580–610 nm when ZnPc content increased to 10 % (Fig. 36B). The fluorescence intensity displayed a first increase and then decrease with the optimal luminous intensity presents in 1.5 % ZnPc/LDH (Fig. 36C). This result indicates an aggregate-induced-quenching process. Moreover, better stability against UV irradiation can be obtained for ZnPc/LDH composites compared with the pristine ZnPc. In addition, the high dispersed ZnPc as monomeric state in the interlayer region of LDH induced by the host–guest and guest–guest interactions can make a big contribution to large singlet oxygen production efficiency in vitro and in vivo photodynamic therapy.

Modulation of the Orientation and Polarized Luminescence

As described above, due to the confined environment of LDHs, interlayer guest molecules possess ordered arrangement and preferred orientation, and thus, the

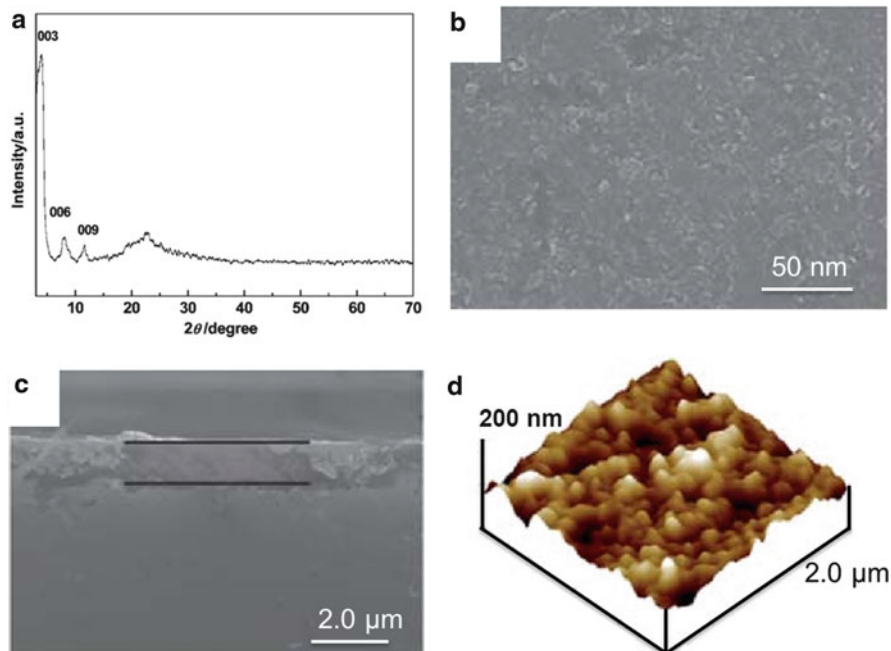


Fig. 37 (a) XRD pattern, (b) top-view SEM, (c) side-view SEM, and (d) tapping-mode AFM images for C3C-DDS/LDH (1.96 %) thin film [110]

obtained LDHs can present polarized luminescence properties. For example, coumarin-3-carboxylate (C3C) and DDS has been co-intercalated into LDH layer, and a C3C-DDS/LDH thin film can be subsequently obtained through solvent evaporation method [110]. Figure 37a shows the sole strong basal reflections (00*l*) for the thin films of C3C-DDS/LDH, indicating a well *c*-oriented assembly of LDH platelets. The uniform and smooth morphology of this film can also be confirmed by top SEM and AFM (Fig. 37b, d). The obtained thin film possesses continuous structure with the average thickness of 1.2 μm (Fig. 37c).

The polarized luminescence of the C3C-DDS/LDH thin films was investigated. Generally, polarized luminescence can be evaluated by determining the anisotropy value *r*, which can be expressed by the formula:

$$r = \frac{I_{\parallel} - I_{\perp}}{I_{\parallel} + 2I_{\perp}} \quad \text{or} \quad r = \frac{I_{VV} - GI_{VH}}{I_{VV} + 2GI_{VH}},$$

where I_{VH} stands for the PL intensity obtained with vertical polarized light excitation and horizontal polarization detection and I_{VV} , I_{HH} , I_{HV} are defined in a similar way; $G = I_{HV}/I_{HH}$ is determined from an aqueous solution of the C3C. Theoretically, the value of *r* is in the range from -0.2 (absorption and emission transition dipoles are perpendicular to one another) to 0.4 (two transition dipoles are parallel

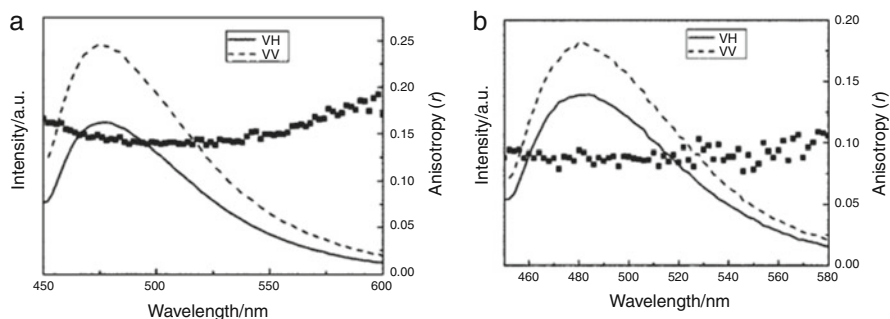


Fig. 38 Polarized fluorescence profiles in the VV, VH modes and anisotropic value (r) for the C3C-DDS/LDH (1.96 %) thin film sample. (a) and (b) correspond to excitation light with glancing and normal incidence geometry, respectively [110]

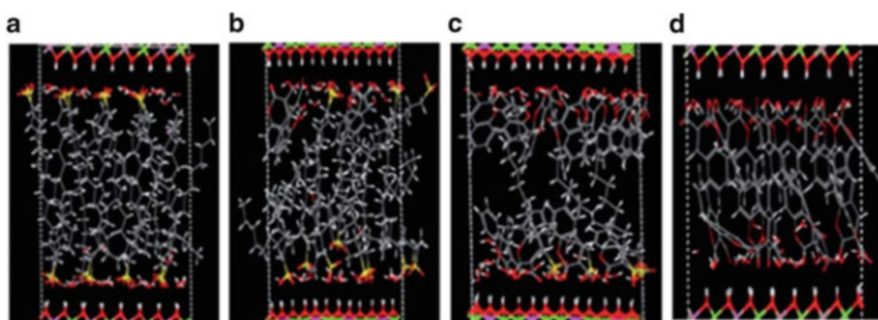


Fig. 39 Snapshots of the simulated equilibrium structures for C3C-DDS/LDHs ($x\%$): (a) 0 %, (b) 25 %, (c) 75 %, (d) 100 % [110]

to each other). The polarized photoemission spectra of the C3C-DDS/LDH (optimal luminous properties was obtained when the content of C3C was 1.96 %) thin film are displayed in Fig. 38. Two typical measurement setups of polarized fluorescence were employed to determine the fluorescence anisotropic value r . It can be observed that the value r is about 0.15 for horizontal excitation (Fig. 38a) and 0.10 for vertical excitation (Fig. 38b), demonstrating highly dispersed and well-oriented arrangement of C3C in the gallery of LDH.

To further investigate variation of the basal spacing influenced by the ratio of C3C/DDS, molecular dynamic simulation was employed to study arrangement and orientation of the C3C anions in the LDH galleries with C3C content ranged from 0, 25, 50, 75, to 100 % (Fig. 39). The results show that the DDS anions under low and high concentration exhibit twisting and stretching state, which severely influence the basal spacing of the C3C-DDS/LDH composites.

Angle θ was defined as the orientational angle of the C3C plane with respect to the LDH layer. It was observed that θ varies between 29 and 55 ° with the most

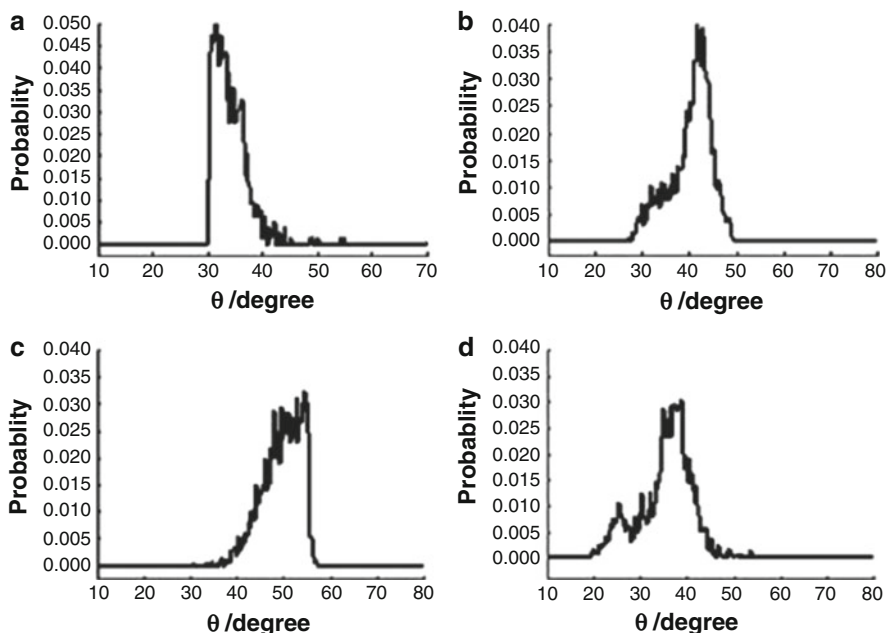


Fig. 40 The distributions of orientational angle θ (the plane of C3C with respect to the LDH layer) with different ratios of C3C to DDS for C3CDDS/LDH ($x\%$): (a) 100 %, (b) 75 %, (c) 50 %, and (d) 25 % [110]

probable angle of ca. 32° for the intercalated C3C ratio at 100 %. Stimulation from Fig. 40 shows that all the C3C molecules are inclining to the layers, attributed to the strong electrostatic interaction between the positive-charged host layers and the C3C anions. The optimal angles of 32° , 42° , and 54° can be obtained when the ratio of DDS and C3C varies from 0 to 1, with a tendency to change from a tilted to a vertical arrangement with respect to the layers. Moreover, the distribution of θ angle for the C3C-DDS/LDH (25 %) with high DDS content corresponds to the relative rigid environment imposed by the DDS which restricts the flexible space for the C3C guest anions. These results show that the changeable interlayer ratio of two components can highly influence the preferred orientation of the photoactive guests.

Several LDH-based LbL thin films also exhibit polarized luminescence properties. Due to the rigid-rod chain configuration or intrinsic one-dimensional structural anisotropy for these luminescent molecules, well-oriented thin films with a macroscopic polarized optical effect can be prepared. For example, sulfonated carbocyanine derivate (Scy) has been assembled with LDH nanosheets, which presents polarized near-infrared (NIR) emission luminescence [100]. The average anisotropy of pristine Scy solution is about 0.2 in the range from 770 to 820 nm, which is related to the random distribution of the dye molecules in the nonviscous liquid. NIR polarized fluorescence with the anisotropic value of ~ 0.8 can be

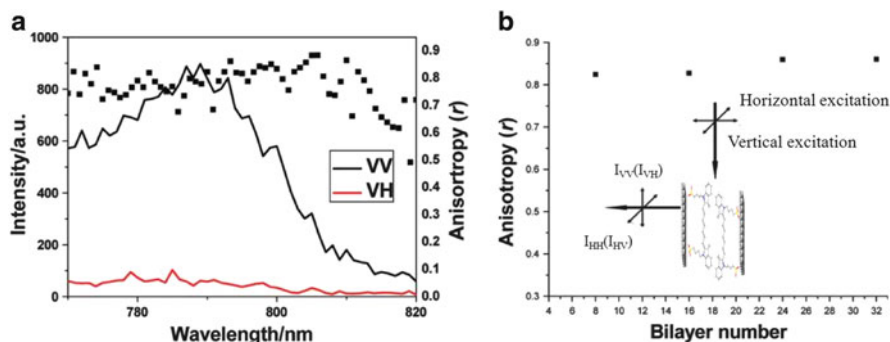


Fig. 41 (a) Polarized fluorescence profiles in the VV, VH modes and anisotropic value r for the (Scy/LDH)₈ UTF. (b) The correlation between fluorescence anisotropic values r of the Scy/LDH UTFs (averaged in the range 770–820 nm) and the bilayer number in the measurement mode with glancing incidence geometry [100]

observed for the Scy/LDH UTF (Fig. 41a), confirming the ordered arrangement of Scy between the LDH nanosheets. There were no obvious changes for UTFs with different number of bilayers (Fig. 41b), indicating the independent macroscopic polarized luminescence on assembly process.

Moreover, due to the regular assembly within the LDH nanosheets, some molecules with no luminescence polarization can also exhibit well-defined anisotropy: the as-mentioned Ru(dpds)₃/LDH UTF is such an example [83]. The pristine Ru(dpds)₃ in aqueous solution shows r at 0.02, while the r value for typical (Ru(dpds)₃/LDH)₃₂ achieved about 0.2–0.3 when comparing the parallel and perpendicular directions to the excitation polarization (I_{VV} vs. I_{VH}) for the in-plane polarized excitation light. Upon increasing the number of bilayers, the r value increases systematically, indicating enhancement of the orderly degree for Ru(dpds)₃ between LDH nanosheets.

Construction of Tunable Multicolor Emissive Film Materials

Materials with multicolor luminescence (especially white-light emission) have been considered as excellent candidates in full-color displays [140], light-emitting diodes (LEDs) [141], and optoelectronic devices [142]. Conventional strategies usually rely on combination of three primary color luminescence species, such as polymers [143], rare-earth compounds [144], metal complexes [145], and semiconductor nanocrystals [146]. However, the different luminous efficiency and intensity, complex fabrication process, as well as complicated interaction between these chromophores have severely limited the development of multicolor materials. Yan et al. [77] have introduced LDH nanosheet as building block to combine different chromophores; in this case, materials with a rigid and ordered microenvironment, finely tuning emission color, and polarized multicolor luminescence can be achieved.

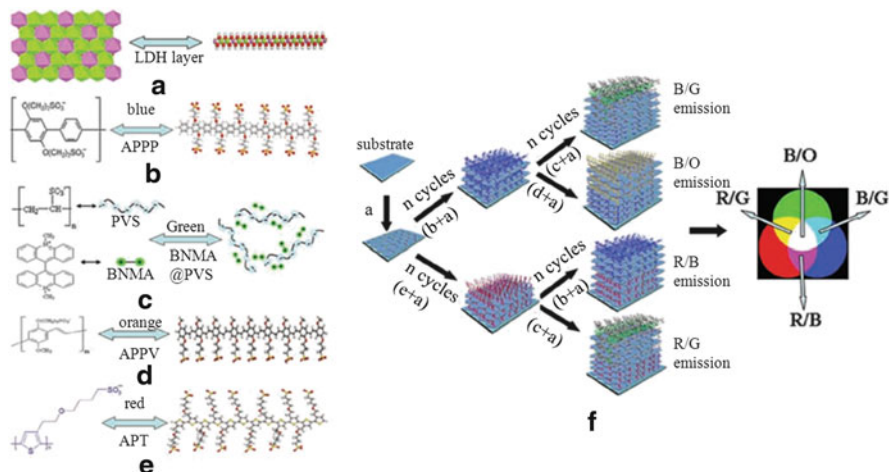


Fig. 42 (a) Representation of one monolayer of MgAl-LDH nanosheet; the chemical formulae of (b) APPP (blue luminescence), (c) BNMA@PVS (green luminescence), (d) APPV (orange luminescence), and (e) APT (red luminescence); (f) procedure for assembling two-color emitting UTFs with blue/green (B/G), blue/orange (B/O), red/blue (R/B), and red/green (R/G) luminescence [77]

Figure 42 shows the assembly process of multicolor emission materials employing APPP (blue) [76], APPV (orange) [78], SPT (red) [79], and BNMA (green) [95] as primary chromophores. The combination of these individual chromophores can obtain organic/inorganic UTFs with emission color throughout the whole visible region, even the white color emission.

Taking $(\text{APPP/LDH})_{12}/(\text{BNMA@PVS/LDH})_n$ ($n = 0-6$) UTFs (B/G luminescence) as the example, the assembly process was carried out by assembling $(\text{BNMA@PVS/LDH})_n$ ($n = 1-6$) bilayers onto the as-prepared $(\text{APPP/LDH})_{12}$ UTF. Figure 43a1 shows the fluorescence monotonic increase at 481 and 504 nm which can be attributed to the emission of BNMA@PVS, while the emission peak at 410 nm is assigned to the pristine $(\text{APPP/LDH})_{12}$ UTF. The similar spectra between assembled UTFs and solutions indicate that the aggregation of BNMA can be avoided throughout the assembly process. The insets show the photographs taken under UV illumination, and high luminescence can be observed for these UTFs. The color coordinates in Fig. 43a2 demonstrated that the color of the UTFs can be tuned from blue (CIE 1931: (0.172, 0.149); $n = 0$) to bluish green (CIE 1931: (0.208, 0.343); $n = 6$) effectively. The multicolor emission of blue/orange, red/blue, and red/green can also be tuned by this method throughout the whole visible region (Fig. 43b-d). In addition, based on the periodic ordered structure of these UTFs, they exhibit well-defined multicolor polarized luminescence with high anisotropy, which may effectively extend its application in multicolor or white polarized photoemission devices.

For the inorganic building blocks, quantum dots (QDs) [147] have attracted great attention due to high quantum yields, good stability, and high color purity [148],

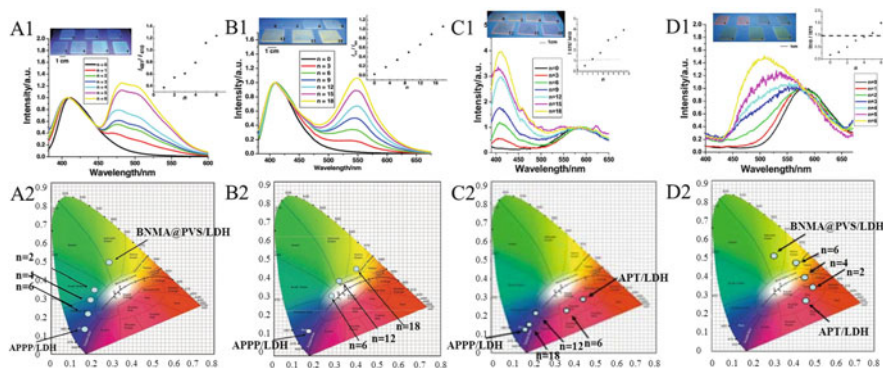


Fig. 43 Fluorescence spectra (the inset shows the ratio of two chromophores), photographs under UV light (365 nm), and the change in color coordinates with n for (a) $(\text{APPP}/\text{LDH})_{12}/(\text{BNMA}@/\text{PVS}/\text{LDH})_n$ ($n=0-6$) UTFs (for B/G luminescence), (b) $(\text{APPP}/\text{LDH})_{12}/(\text{APV}/\text{LDH})_n$ ($n=0-18$) UTFs (for B/O luminescence), (c) $(\text{APPP}/\text{LDH})_{12}/(\text{APT}/\text{LDH})_n$ ($n=0-18$) UTFs (for R/B luminescence), and (d) $(\text{APT}/\text{LDH})_{12}/(\text{BNMA}@/\text{PVS}/\text{LDH})_n$ ($n=0-6$) UTFs (for R/G luminescence) [77]

and application of QDs in the multicolor emission materials has also been carefully investigated. Liang et al. [117] have assembled QDs with LDH nanosheets to obtain highly ordered structure and finely tunable fluorescence, and the tunable color in the red–green region could be achieved by adjusting the assembly cycle number and sequence of red- and green-emission QDs. In addition, Tian et al. [102] have introduced fabrication of precisely tuned white color emission UTFs employing red- and green-emission QDs and blue 2,2'-(1,2-ethenediyl) bis [5-[[4-(diethylamino)-6-[(2,5-disulfophenyl) amino]-1,3,5-triazin-2-yl] amino] benzene-5 sulfonic acid] hexasodium salt (BTBS). By adjusting the deposition sequence and relative ratio of the blue-, green- and red-emission units, luminescent UTFs with finely tunable photoemission in the white spectral region were obtained (Fig. 44B). Moreover, the color coordinates of the best white-light emission (denoted as f in Fig. 44C) could achieve (0.322, 0.324) which is very close to the standard coordinates of white light (0.333, 0.333).

The emission color of hybrid composites can be tuned in response to different excitation light, which has been recognized as an intelligent photoluminescence material. This composite UTF was illustrated as $(\text{BTBS}/\text{LDH})_{12}(\text{QD-530}/\text{LDH})_{20}(\text{QD-620}/\text{LDH})_7$, composed of three chromophores: red-emission and green-emission QDs and blue-emission organic compound BTBS. Due to the different excitation and emission spectra of these three chromophores, it can be concluded that BTBS can be excited at 360 nm while photon energy above 500 and 600 nm can efficiently excite QD-530 and QD-620. Therefore, excited at 360, 460, and 560 nm, the UTFs display three different emission spectra as well as corresponding white, orange, and red color, respectively (Fig. 45). These hybrid materials responding to external excitation light via the alteration of emission color can be widely used in anti-forgery, colorimetric sensors, and display devices.

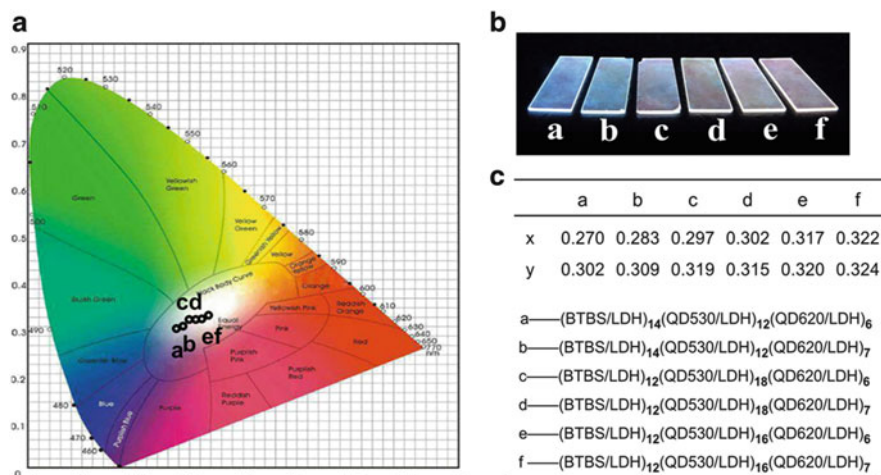


Fig. 44 Optical spectroscopy characterization of the $(\text{BTBS/LDH})_m(\text{QD-530/LDH})_n(\text{QD-620/LDH})_p$ UTfs: (A) the change in color coordinates in the *white-light* region, (B) their photographs under UV light (365 nm), (C) the color coordinates and detailed compositions of these UTfs [102]

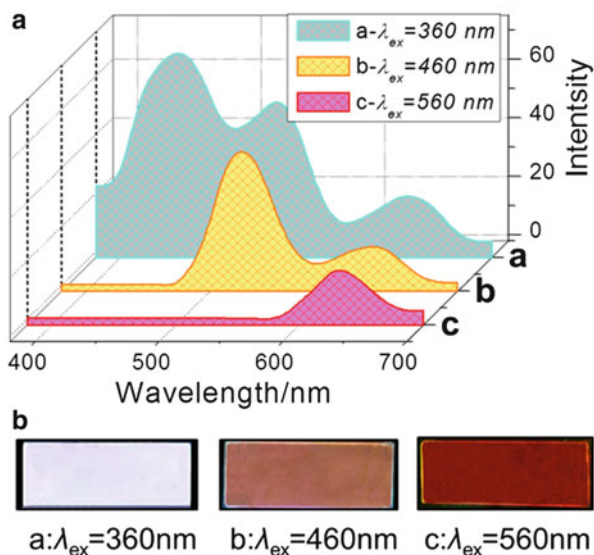


Fig. 45 (A) The emission spectra, (B) photographs of the $(\text{BTBS/LDH})_{12}(\text{QD-530/LDH})_{20}(\text{QD-620/LDH})_7$ UTf with different excitation wavelength: (a) excited at 360 nm, (b) excited at 460 nm, (c) excited at 560 nm, respectively [102]

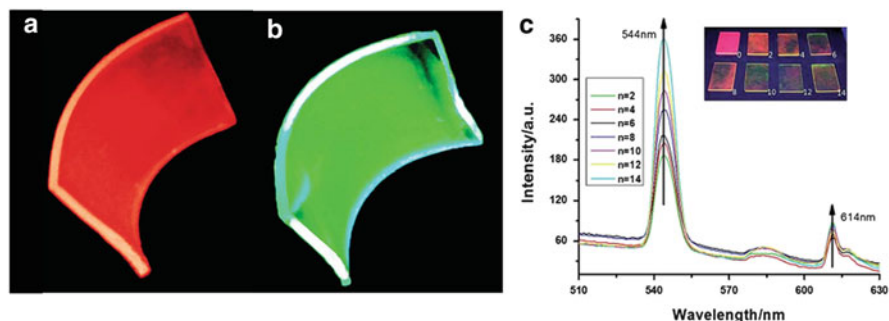


Fig. 46 Digital photos of flexible (a) $(\text{Eu}(\text{DBM})_3\text{bath}/\text{LDH})_8$ and (b) $(\text{Tb}(\text{acac})_3\text{Tiron}/\text{LDH})_8$ UTFs under UV irradiation; (c) fluorescence spectra of $(\text{Eu}(\text{DBM})_3\text{bath}/\text{LDH})_{10}/(\text{Tb}(\text{acac})_3\text{Tiron}/\text{LDH})_n$ ($n = 0-14$) UTFs, and insets show the photographs under UV light [149]

Moreover, sulfonated Eu- and Tb-based lanthanide complexes can also be employed in fabrication of multicolor emission materials [149]. After the synthesis of red-emissive $\text{Eu}(\text{DBM})_3\text{bath}$ and green-emissive $\text{Tb}(\text{acac})_3\text{Tiron}$ (DBM, dibenzoylmethane; bath, bathophenanthroline disulfonate disodium; acac, 2,4-pentanedione), these lanthanide complexes can be assembled with LDH to obtain highly emissive luminescence with tunable color on tuning of their relative ratio (Fig. 46). In addition, these UTFs exhibit well-defined one and two-color polarized fluorescence and obvious red and green up-conversion emission upon excitation by near-IR laser light.

6.3.2 Dynamic Tuning of the Emission

The photofunctional materials with smart-responsive properties can present dynamic changes by tuning the external stimuli. Such dynamic-responsive photofunctional materials should have rapid response time, high sensitivity, obvious signal change, and high stability for long-term use [150]. In order to achieve these requirements, LDHs have been employed as an effective inorganic matrix and building block for the ordered arrangement and improved stability of active chromophores in the solid state [151]. Recently, the smart-responsive LDH photofunctional materials responding to environmental stimuli (such as chemical substances, pH value, temperature, pressure, light irradiation, and electricity) have been studied, which present dynamic tuning of their photofunctionalities.

Detection of Chemical Substances

Chemo-sensor plays an important role in the detection of heavy metal ions (HMIs), biomolecules, environmental pollutants, and chemical warfare agents [152–156]. The basic mechanisms of fluorescence detection for most of hazardous substances

rely on the quenching induced by the binding between analytes and fluorescence probe molecules. However, the commonly studied fluorescence probe molecules are in aqueous or powder states, and the complicated operation process and difficulty in recyclability have severely limited the application of such materials. Therefore, the development of suitable species and/or new approaches toward the facile fabrication of chemo-sensor with high sensitivity, fast response, and decent recyclability remains a stimulating challenge.

Fabrication of photofunctional UTFs based on the LbL assembly with LDH nanosheets can serve as an effective method to solve the above difficulties. A certain amount of fluorescence molecules have been applied (such as BTBS [101], calcein [109], and 1-amino-8-hydroxy-3,6-disulfonaphthalene (H-acid) [157]) as probes for the detection of HMIs (such as mercury ion). Taking BTBS/LDH system as an example, fluorescence emission spectrum shows a monotonic increase with n at ca. 445 nm, and the UTFs show well-defined blue luminescence under UV light (Fig. 47a and inset). The systematical and significant photoemission decrease of the (BTBS/LDH)₃₂ UTF can be observed in responding to the addition of Hg²⁺ (Fig. 47b), while different degrees of quenching for metal ions were presented in Fig. 47d. The strongest quenching by Hg²⁺ is related to the high thermodynamic affinity with typical O-chelate ligands and metal-to-ligand binding kinetics. Reproducibility was carried out for alternative dipping the UTFs into Hg²⁺ and EDTA, and the UTFs can recover to the pristine fluorescence intensity at least five cycles (Fig. 47c). The immobilization by LDH has guaranteed the repeatability of HMI detection, while the drop-casted sample is easy to fall off in solution.

Moreover, Jin et al. have proposed the detection of biomolecules dextran-40 by employing 8-amino-1,3,6-naphthalenetrisulfonates (ANTS) and LDH as building block [158]. The obtained (ANTS/LDH)_{*n*} UTF can be adapted in the detection of Mg²⁺ which is important in stabilizing the structure of DNA and transferring of biological signals [159]. The detection limit of 2.37×10^{-7} M can be obtained. Trinitrotoluene (TNT), which is an important explosives commonly applied in both military and forensic science, can be specifically detected by (BBU/LDH)_{*n*} UTFs, which are assembled by 4,4'-bis[2-di(b-hydroxyethyl)amino-4-(4-sulfophe-nylamino)-s-triazin-6-ylamino] stilbine-2,2'-disulfonate (BBU) with LDH nanosheets [103].

Li, Qin, and coworkers have efficiently detected the volatile organic compounds (VOCs) based on modulating the FRET process. The basal spacing and the interlayer distance between donor and acceptor can be varied with external stimuli (VOC vapor), and thus, the color change from blue to violet can be observed for the detection [93, 135].

pH Sensor

Optical pH sensor with stable lifetime and signal is of great importance in environmental research, toxicological assay, blood measurement, and biotechnology [160–163]. The red-emissive (SPT/LDH)₃₂ UTF described above exhibited reversible responses toward pH in alternative dipping in aqueous at pH = 4 and pH = 13 [79].

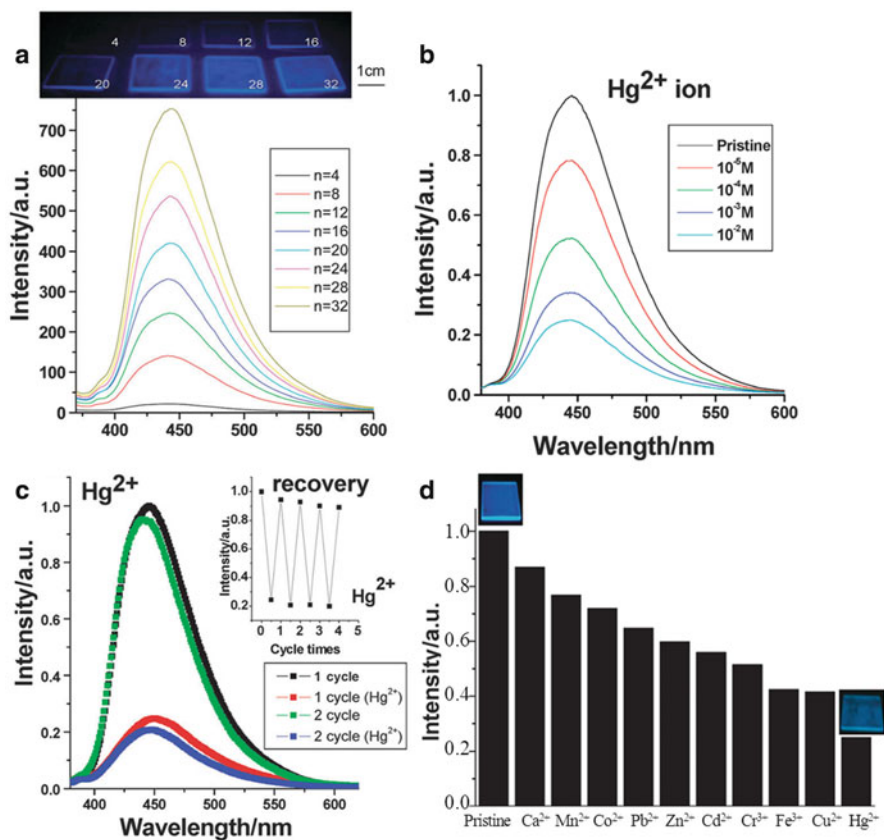


Fig. 47 Fluorescence spectra of the $(\text{BTBS/LDH})_{32}$ UTFs for (a) variation in bilayer number (inset shows the photograph under UV light), (b) treated with Hg^{2+} at different concentration, and (c) detecting the Hg^{2+} after alternate treatment by metal ions and EDTA aqueous solutions over continuous reversible cycles (the inset shows the fluorescence intensities over five cycles); (d) comparison of the normalized luminescence intensity of the UTF responding to aqueous solutions of different metal ions (10^{-2} M) [101]

It has been found that dipping the $(\text{SPT/LDH})_{32}$ UTFs in aqueous solutions with different pH values ranging from 4 to 14 for 10 s is sufficient for the proton to transfer into the UTFs, and the UTFs can display a variation of maximum emission wavelength (Fig. 48a). This result can be attributed to the occurrence of protonation and deprotonation of SPT between the LDH nanosheets. Reproducibility was also carried out in alternation between pH = 4 and pH = 13 for five cycles (Fig. 48b), and rapid change from bright red luminescence at pH = 13 to dark orange at pH = 4 can be observed under UV light (365 nm).

Shi et al. have fabricated another pH sensor based on the co-intercalation of the fluorescein (FLU) and 1-heptanesulfonic acid sodium (HES), and the obtained samples exhibit good photo- and storage stability as well as high repeatability

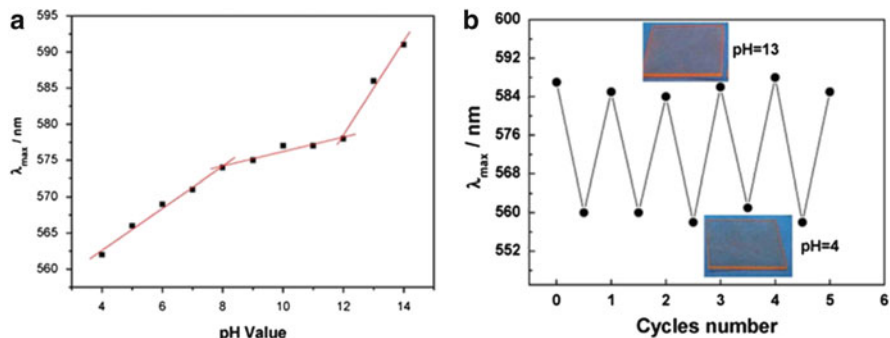


Fig. 48 (a) Variation of the maximum photoemission wavelength of the (SPT/LDH)₃₂ UTF with different pH values and (b) the reversible photoemission response upon alternation between pH = 4 and pH = 13 (the inset show the luminescence photographs of the UTFs at the two pH conditions) [79]

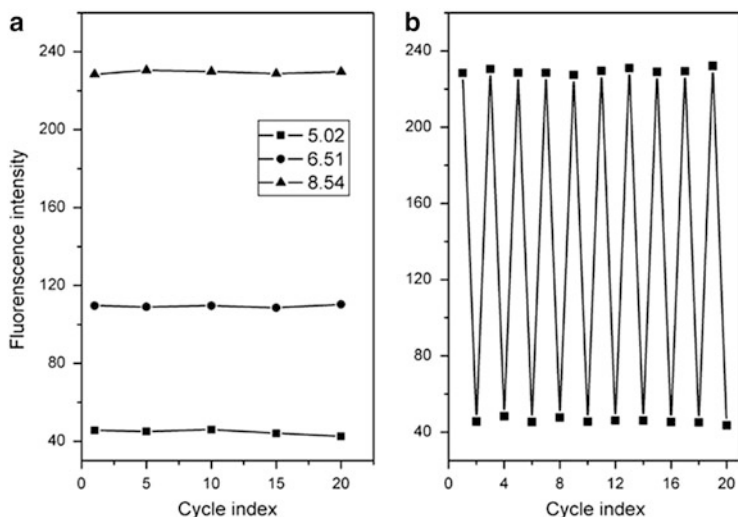


Fig. 49 (a) Fluorescence intensity of the pH sensor recorded after 1, 5, 10, 15, and 20 cycles at pH 5.02, 6.51, and 8.54 and (b) the reversibility recorded by alternate measurement in two solutions with pH 5.02 and 8.54 [106]

toward responses of pH [106]. Employing electrophoretic deposition method, a sensor with broad linear dynamic range in pH (5.02–8.54) can be obtained (Fig. 49a). Remarkable repeatability in 20 cycles can be achieved with the relative standard deviation (RSD) less than 1.5 % (Fig. 49b). The sensitive and rapid responses of SPT/LDH and FLU/LDH toward pH materials indicated their potential application as pH luminescence sensor.

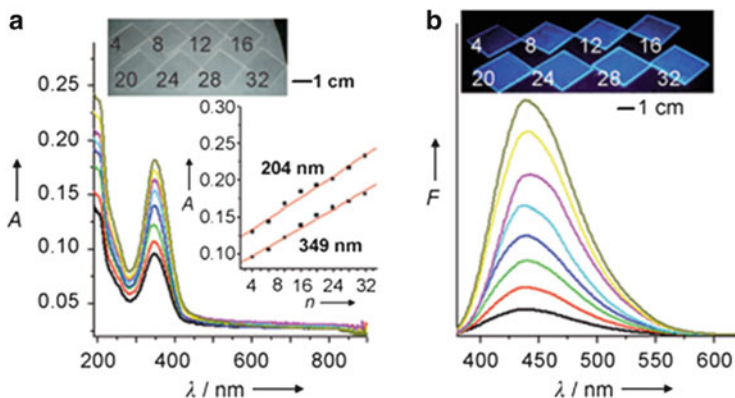


Fig. 50 Characterization of $(\text{BSB/LDH})_n$ ($n=4\text{--}32$) UTFs. (a) UV–Vis absorption spectra (inset: plots of the absorbance at 204 and 349 nm vs. the number of bilayers n) and (b) fluorescence spectra. The insets in (a) and (b) are photographs of UTFs with different n under daylight and UV light (365 nm), respectively [99]

Temperature Sensor

Temperature is one of the most common and natural environmental factor, and thermochromic materials can be potentially used in temperature sensor and devices [164–166]. Therefore, much attention has been paid on fabrication of thermochromic materials with good sensitivity and reversibility. Bis (2-sulfonatostyryl)biphenyl (BSB) was employed as thermochromic luminescence (TCL) molecule to assemble with LDH nanosheet to achieve an ordered supramolecular UTFs [99]. Figure 50 shows the assembly process of $(\text{BSB/LDH})_n$ with the monotonic increase in absorption and fluorescence emission spectra. The maximum emission peak is located at 444 nm, and no broadening or shift can be observed in the whole assembly process, indicating no interaction between molecules occurred. The XRD data show the ordered and monolayer arrangement of BSB in the interlayer of LDHs.

The TCL behavior of the UTFs was studied on heating from 20 to 100 °C, and a gradual decrease in fluorescence intensity with a red shift from 444 to 473 nm can be observed (Fig. 51a). A visible change can be observed under UV light with the emission color changes from blue to bluish green upon heating. The recover in color and spectrum can be accomplished when the UTF cooled to 20 °C, and this heating–cooling process can be readily repeated (Fig. 51a, inset). Fluorescence lifetimes of these $(\text{BSB/LDH})_n$ UTFs were also studied to obtain the excited-state information. The results show that lifetime of the UTF is longer at 100 °C (1.9 ns) than that at 20 °C (0.9 ns), and the recycle can also be achieved (Fig. 51b). Figure 51c shows the polarized fluorescence measurements of the UTFs, and the degree of structural order can be obtained by detecting the fluorescence anisotropy r . The r value decreases from 0.15 at 20 °C to 0.02 for UTFs at 100 °C, which exhibit a less ordered arrangement of molecules at high temperature.

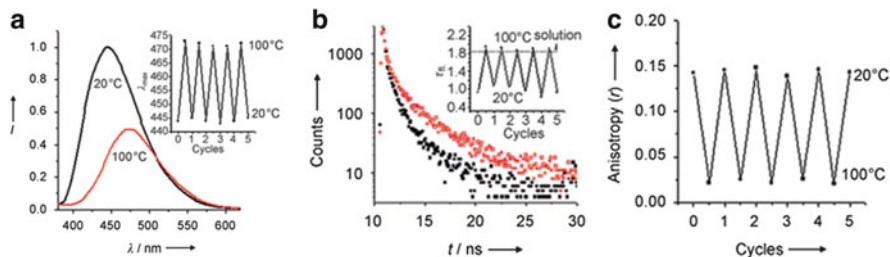


Fig. 51 TCL of the $(\text{BSB/LDH})_8$ UTF at 20 and 100 °C. (a) Fluorescence emission spectra (inset: the reversible fluorescence response over five consecutive cycles); (b) typical fluorescence decay curve (inset: fluorescence lifetimes over five consecutive cycles, *black*: 20 °C, *red*: 100 °C); (c) fluorescence anisotropy over five consecutive cycles [99]

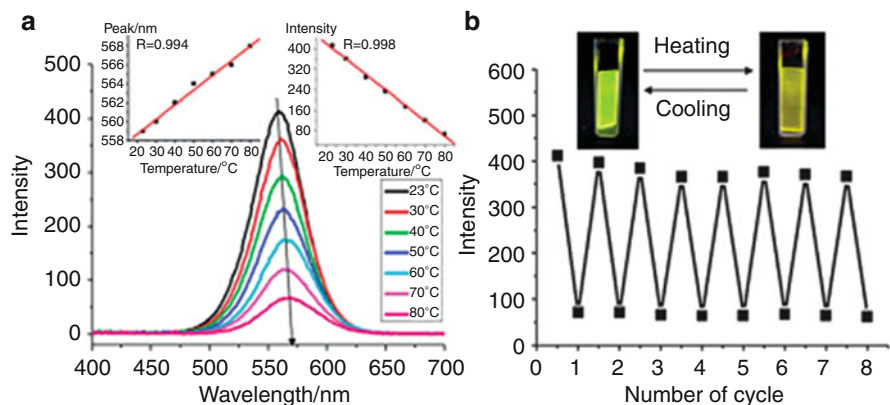
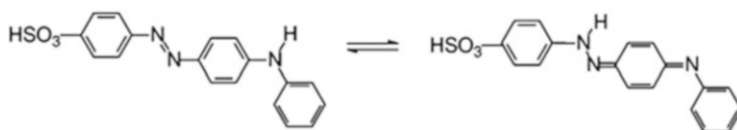


Fig. 52 (a) The luminescence spectra of the $(\text{CdTe QDs/LDH})_{30}$ UTF in the temperature range 23–80 °C (inset: the emission position or intensity as a function of temperature, respectively); (b) the reversible fluorescence response of eight consecutive cycles (the inset shows the UTF photographs at 23 and 80 °C, respectively) [116]

Similar observations can also be obtained for $(\text{CdTe QDs/LDH})_{30}$ UTF [116]; Fig. 52a shows the responses toward temperature upon heating, and an intensity decrease along with red shift can be observed. These inorganic–inorganic hybrid UTFs possess good sensitivity, and -1% per °C decrease and $0.1\text{ nm }^\circ\text{C}^{-1}$ red shift can be obtained. The UTFs exhibit excellent repeatability for eight cycles in the heating–cooling process (Fig. 52b).

Aromatic azo dyes, such as 4-(4-anilinophenylazo)benzenesulfonate (AO5), have been widely used due to the easy transformation between the azo A-form and hydrazone H-form (Scheme 3). It was well known that this tautomerism is very sensitive to the surrounding environment; therefore, it has been widely used as thermal sensors and in molecular memory storage. In order to further modulate the environment in an inorganic matrix, AO5 was co-intercalated with sodium dodecylbenzene sulfonate (SDS) into the interlayer of LDH [112]. The absorption



Scheme 3 Tautomeric equilibrium between the A-Form and H-Form of AO5 [112]

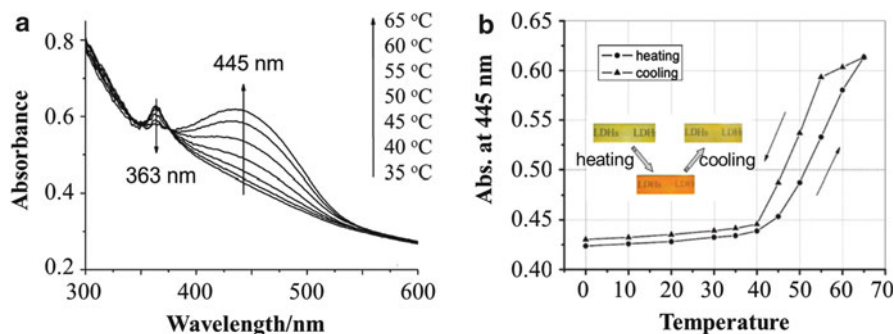


Fig. 53 (a) In situ absorption spectra of the 10 % AO5-LDH film during heating in the range 35–65 °C. (b) The correlation between the absorbance of the band at 445 nm and temperature over a complete heating–cooling cycle (inset shows the corresponding digital photographs) [112]

band at 363 nm at room temperature is attributed to the absorption of A-form, and the intensity increases with elevated temperature (Fig. 53a). The color of the composite film exhibits reversible change from light yellow to orange in the range of 35–65 °C, which is in accordance with absorption at 445 nm. Since the pristine AO5 shows no thermal-responsive behavior, this thermochromic phenomenon for the UTF can be a result of tautomerism of interlayer AO5 and changes in host–guest and guest–guest interactions.

In addition, thermal colorimetric and fluorescent response behaviors of polydiacetylene (PDA) in the LDH layers were also studied [81]. Diacetylene (DA) was firstly intercalated into the interlayer of LDHs, and subsequent PDA/LDH films were fabricated through UV-induced polymerization of intercalated DA. And the reversible changes under both visible light and UV light can be observed in the temperature range of 20–130 °C. This phenomenon can be attributed to the influence of hydrogen bond formed between LDH layers and PDA guests.

Pressure Sensor

Pressure-induced chromic, known as piezochromic, is an interesting phenomenon for luminescence materials responding to natural external force [167]. However, the research on piezochromic luminescent (PCL) materials remains relative seldom

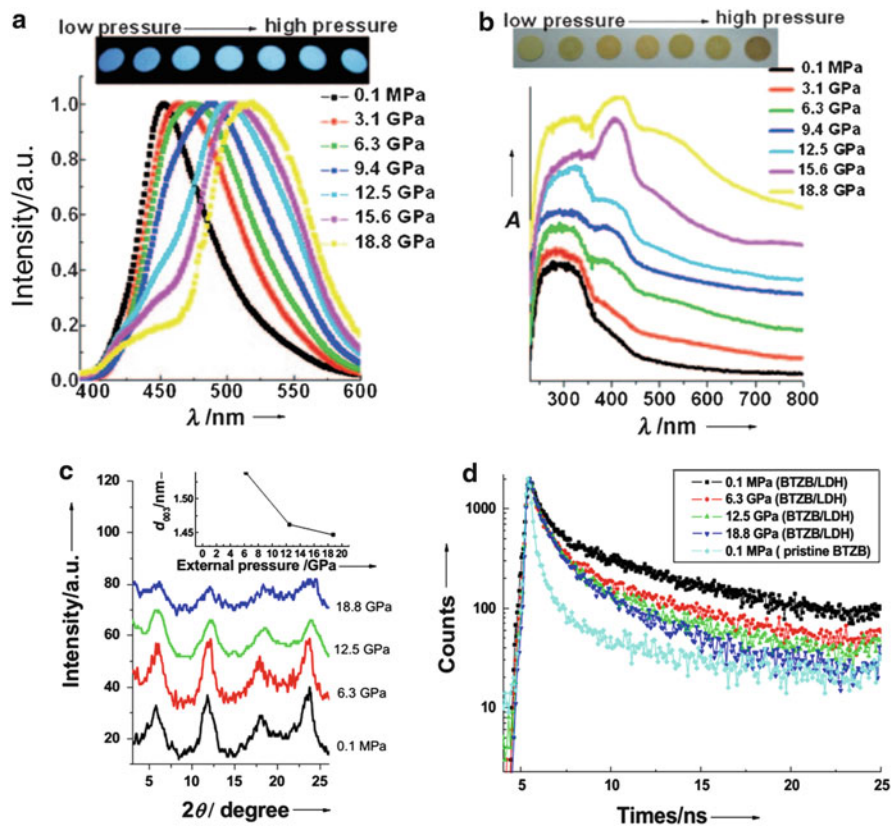


Fig. 54 (a) Fluorescence emission and (b) UV-Vis spectra of the BTZB/Mg₂Al-LDH at different pressures (inset shows the photographs of pressurized samples under daylight and UV light, respectively); (c) XRD pattern with the varying interlayer distance and (d) fluorescence lifetime of the BTZB/Mg₂Al-LDH at different pressures [111]

compared with other environment-responsive materials (such as temperature-, pH- and HMI-sensitive materials). Therefore, the investigation on PCL materials with excellent reversibility, repeatability, and rapid responsiveness is still a challenge [168, 169].

Yan et al. have studied the fluorescence properties as well as molecular packing mode of (2,2'-(1,2-ethenediyl)bis[5-[[4-(diethylamino)-6-[(2,5-disulphophenyl)amino]-1,3,5-triazin-2-yl] amino]benzene sulfonate anion (BTZB) after intercalation into LDHs matrix [111]. The fluorescence of the pristine BTZB and BTZB/LDH composites is shown at approximately 452 nm, and significant luminescent changes can be observed for the BTZB/LDHs treated with pressures while pristine BTZB remains unchanged. Figure 54a shows the changes of fluorescence spectra upon increasing the pressure from 0.1 MPa to 18.8 GPa; the emission wavelength shifts from 452 to 515 nm, which can be assigned to the formation of *J*-type

aggregates in the LDH galleries. The change of this phenomenon can be obviously seen from photographs of the BTZB/LDH pellet under UV light (Fig. 54a, inset) with the color varies from blue to green with increasing pressure. UV–Vis spectra also exhibit an obvious change on varying the pressure (Fig. 54b). Except for the absorption band at 290 nm for the pristine BTZB/LDH, a new band, ranging from 350 to 450 nm, appears when the pressure is sustainably increased. A broad shoulder band at 450–550 nm can be observed when the pressure was increased to 15.6 GPa. The appearance of this new band is due to the formation of *J*-type aggregates of BTZB in the interlayer of LDH, which is in accordance with the results from fluorescence tests above. In order to take an insight into the influences of pressure on the supramolecular organization in this BTZB/LDH host–guest system, XRD was carried out. Figure 54c shows that upon increasing the pressure from 0.1 MPa to 18.8 GPa, the basal d_{003} spacing changes from 1.57 to 1.45 nm, maintaining the structure of LDHs. This may be due to the contracted gallery height and subsequent rearrangement of intercalated guest molecules. And the fluorescence lifetime of BTZB/LDH is much shorter at high pressure (2.14 ns at 18.8 GPa and 4.63 ns at 0.1 MPa), further confirming the aggregation of the BTZB (Fig. 54d).

Reversibility and repeatability tests are also carried out by grinding and subsequent heating for the pellet sample, and a reversible performance for practical application of PCL materials is satisfactorily obtained. Moreover, the different composition of host layer has been investigated, and the results show that $\text{Mg}_2\text{Al-LDH}$ possesses better PCL performances compared to Zn-Al-LDH or $\text{Mg}_3\text{Al-LDH}$. Therefore, these BTZB/LDH materials exhibit obvious changes in UV–Vis absorption, fluorescence emission, and lifetime upon the increase of pressure, and the color change from blue to green under UV light can be visually seen. Theoretical results show that the variations of the arrangement and aggregation status of BTZB in the interlayer of LDH cause the subsequent PCL phenomenon.

Mechanofluorochromism can be observed in the NFC-HPS (NFC, niflumic acid, a typical aggregation-induced emission molecule; HPS, heptanesulfonate) co-intercalated LDHs [170]. The results show that NFC-HPS/LDH (HFC: HPS = 5 %) possesses obvious change in fluorescence on mechanical force, while the pristine solid-state NFC sample remains nearly unchanged under pressure. This phenomenon can be attributed to the slipping of LDH sheets and reorientation of the interlayer surfactant; and the changed host–guest interactions can tune the molecular conformation and intermolecular interaction of NFC anions.

Light-Induced Sensor

Photochromism is a phenomenon that substance exhibits color change upon light irradiation, and it has been widely used in light switching, liquid-crystal alignment, information storage, and nonlinear devices [171–173]. It is well known that the photoisomerization process is very sensitive to the surrounding microenvironment, and the low isomerization efficiency and stability has limited the development of photochromic materials. Embedding the photo-responsive molecules into the

inorganic matrix, such as LDH nanosheets, may effectively inhibit the aggregation of the molecules and thus enhance the photoisomerization free space for photochromism.

Wang et al. have studied the photoisomerization process of a kind of Schiff base (azomethine-H anions, AMH) assembled LDH system [174]. Generally, after the excitation of the initial enol (anti-enol) tautomer, the excited-state intramolecular proton transfer (ESIPT) occurs for AMH, leading to the excited keto tautomer (cis-keto or its zwitterionic form), exhibiting a characteristic Stokes fluorescence band. After the structural changes (rotation around C=C and/or C-N bond) involving the cleavage of the intramolecular hydrogen bond, the red long-lived photochromic tautomer (trans-keto or its zwitterionic form) in the ground state is generated either by thermal treatment or by irradiation of visible light.

In order to obtain advanced performance along with good stability, AMH was co-intercalated with 1-pentanesulfonate (PS) into the interlayer of LDH, and the corresponding thin films of AMH/PS-LDH were obtained by the solvent evaporation. Firstly, the photoisomerization process of the pristine AMH solution has been studied, and the transient absorption spectra were illustrated in Fig. 55a. The bands at 470 nm are attributed to the absorption from the S_0 state of the trans-keto tautomer, and the band with a maximum at ~ 370 nm is possibly related to the long-lived syn-enol form. Upon irradiation of laser, a dramatic decrease can be observed. For AMH/PS-LDH films, an excited-state intramolecular proton transfer to the trans-keto tautomer was occurred when the initial AMH (as an enol tautomer) receives UV excitation, and the relaxed back isomerization to the ground state was observed through transient UV-Vis spectroscopy (Fig. 55b). The band located at 465 nm is due to the S_0 state of the trans-keto tautomer, and a 5 nm blue shift due to the changed weak polar microenvironment can be observed. The absence of syn-enol form indicates the inhibition of the syn-enol/anti-enol isomerization in the

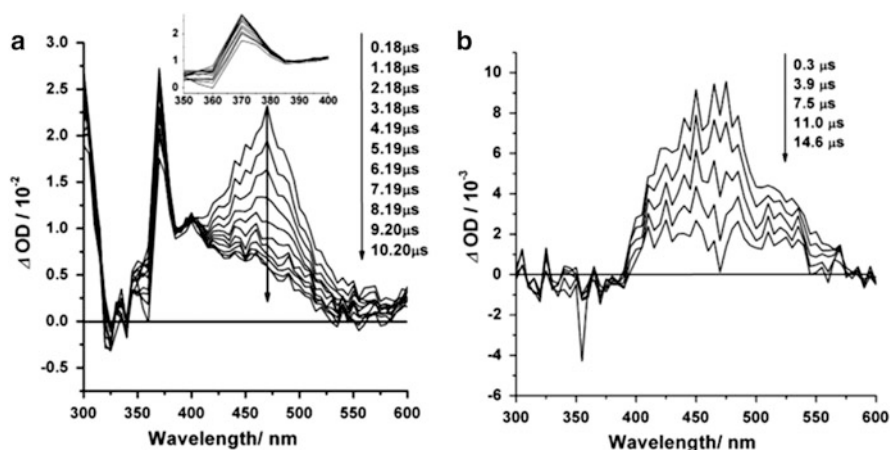


Fig. 55 Transient absorption spectra obtained by laser photolysis for (a) nitrogen-saturated solution of AMH (5.0×10^{-5} M) in water (inset shows the magnified absorption from 350 to 400 nm), and (b) the 2 % AMH-LDH film [174]

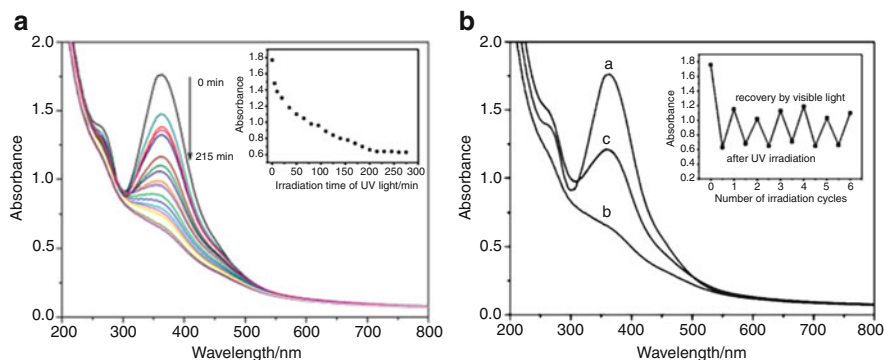


Fig. 56 UV-Vis absorption spectra of photoisomerization for the (LDH/PAZO)₅₀ film: (A) the absorption intensity changes with time; (B) repeatability tests for (a) the *trans* isomer, (b) the same sample after irradiation with UV light, and (c) the recovered *trans* isomer after irradiation with visible light. The inset shows the change in the absorbance at the maximum of 376 nm [82]

2D confined environment. As a result, the *trans*-keto tautomer of AMH is less stable in the 2D confined environment, and relaxed back isomerization is more easily to take place.

Moreover, photoactive azobenzene polymer PAZO was also applied in the assembly with LDH to obtain a photochromism material [82]. Upon UV irradiation, the absorption at 376 nm decreases as a function of time (Fig. 56A) due to the transformation of *trans* to *cis* of PAZO. A complete isomerization can be achieved (Fig. 56B, line *a*–*b*) after sufficient irradiation time. The π – π^* absorption band increases again (Fig. 56B, line *c*) when irradiated by visible light ($\lambda > 450$ nm), and the back isomerization for the *cis*–*trans* can be achieved. The extent of 51 % is obtained for the *cis* to *trans* back isomerization, and repeatability for several cycles can be accomplished by alternative irradiation of UV and visible light. The results show that the intertwisting of polymer chains and π – π stacking of the azobenzene chromophores can be efficiently reduced, and sufficient free space is available for the isomerization of the azobenzene moiety due to the employment of LDH nanosheets.

Light-triggered materials containing porphyrin and phthalocyanine molecules for biological and medical application were also largely investigated. Through the intercalation, the inherent properties of these porphyrin and phthalocyanine molecules may be altered [175]. [Tetrakis(4-carboxyphenyl)-porphyrinato]zinc (II) (ZnTPPC) [88], Pd(II)-5,10,15,20-tetrakis(4-carboxyphenyl) porphyrin (PdTPPC) [89], 5,10,15,20-tetrakis(4-sulfonatophenyl) porphyrin (TPPS), and its palladium complex (PdTPPS) [89–91] intercalated LDH-based hybrid materials have been studied. Figure 57 shows the relaxation of PdTPPS phosphorescence (triplet states) and luminescence signals of $O_2(^1\Delta_g)$ in the assembled LDH-DS/PdTPPS films. The proximity of the porphyrin triplet states and their interaction with $O_2(^1\Delta_g)$ contribute to the repopulation of the fluorescent excited singlet states of TPPS. Moreover, Liang et al. have also studied the singlet oxygen production

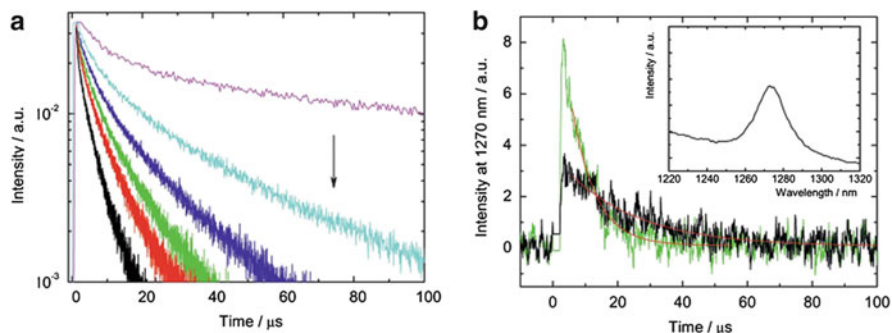


Fig. 57 (a) Quenching of the PdTPPS triplet states in the $\text{Mg}_2\text{Al-LDH-DS/PdTPPS}$ film at different oxygen pressures (excitation at 425 nm, phosphorescence recorded at 690 nm); the arrow shows increasing O_2 pressure (vacuum, 100, 210, 300, 400, 760 Torr). (b) Time dependencies of the $\text{O}_2(^1\Delta_g)$ luminescence signals in air (black line) and oxygen (green line) after the excitation of TPPS in the $\text{Mg}_2\text{Al-LDH-DS/TPPS}$ film. The red lines are least-squares monoexponential fits (inset shows emission band of $\text{O}_2(^1\Delta_g)$ in air) [91]

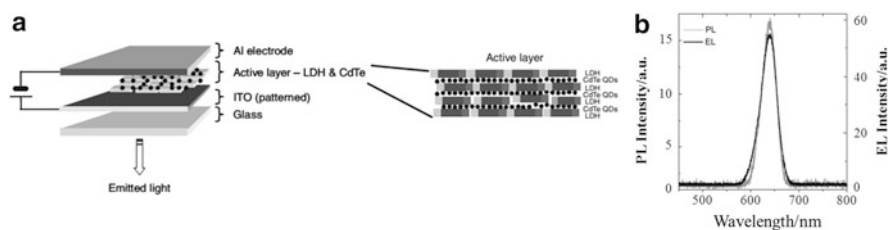


Fig. 58 (a) Schematic of the architecture of the device, which is based on a “sandwich” structure, and (b) photoluminescence peak of aqueous CdTe QDs (gray curve) compared to the electroluminescence peak of the device (black curve) [119]

efficiency of zinc phthalocyanines intercalated LDHs, and the composite materials exhibit excellent anticancer behavior when used for photodynamic therapy [92].

Electroluminescence, Chemiluminescence, and Electrochemiluminescence

Electroluminescence (EL) is the luminescent behavior induced by external electric field, which requires saturated emission colors, high thermal stability, and long operational lifetimes of chromophores [176]. However, traditional EL devices often suffered from low efficiency, short lifetimes, and complicated fabrication technique under specially controlled environment. A method for fabricating high efficiency and thermally stable light-emitting device (LED) involving simple technique is quite needed. Bendall et al. [119] have designed an all-inorganic EL device constructed by assembly highly luminescent CdTe QDs with LDH nanosheet (Fig. 58a). EL emission peak, which can be observed at 637 nm, is almost the

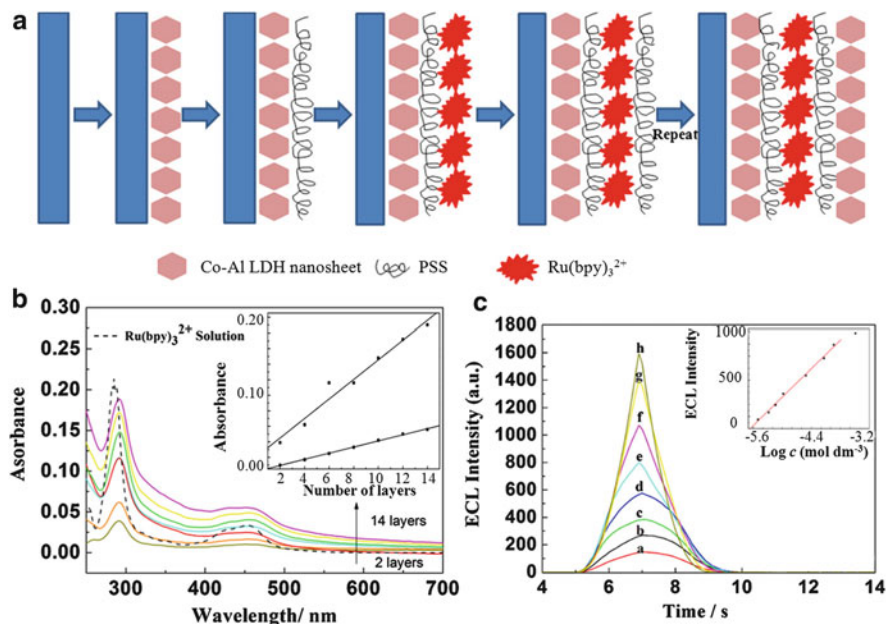


Fig. 59 Assembly and properties of $(\text{LDH}/\text{PSS}/\text{Ru}(\text{bpy})_3^{2+}/\text{PSS})_n$ multilayer films: (a) schematic representation, (b) UV-Vis absorption spectra along with different tetra-layer number n (the inset shows the absorbance at 291 and 457 nm vs. n), and (c) ECL spectra in the presence of NADH with various concentrations (from a to h: 3.16×10^{-6} to 3.23×10^{-4} M, scan rate = 100 mV s^{-1} , and the inset shows plot of ECL intensity vs. NADH concentration) [179]

same as the photoluminescence (PL) emission peak of the bare QD without any shift or broadening occurs. Such device maintains the requirements for the common organic LEDs, and possesses better thermal stability (can be operated over 80°C) due to the employment of LDHs. Thus, a bright, monochrome, and stable EL device with excellent thermal stability, brightness, and simple fabrication process is achieved.

Chemiluminescence (CL) stands for the luminescence derived from a chemical reaction. Much attention has been paid on enhanced CL for detection in biology and sensor fields [177]. Lu et al. have investigated the CL phenomenon based on nanocomposite material constructed by the assembly of CdTe QDs upon the surface of DBS-LDHs in an ordered manner. The obtained material exhibited a remarkable CL amplification of the luminol- H_2O_2 system due to ordered arrangement of QDs and host-guest interaction between LDH and CdTe QDs [121].

Electrochemiluminescence (ECL) is a combined process of EL and CL, which is caused by energetic electron transfer (redox) reactions of electrogenerated species [178]. Recently, ECL based on a solid-state sensor has also been investigated employing ruthenium(II) tris(bipyridine) and poly(sodium 4-styrene sulfonate) to assemble with LDH nanosheets [179]. Figure 59a shows the assembly process for

this (LDH/PSS/Ru(bpy)₃²⁺/PSS)₁₀ multilayer films, and UV–Vis spectra has been used to monitor the stepwise growth of the UTFs (Fig. 59b). A linear response to dihydronicotinamide adenine dinucleotide (NADH) in the range 3.16×10^{-6} to 3.23×10^{-4} M can be obtained, and the detection limit can reach as low as 0.023 μ M (Fig. 59c).

Therefore, the application of LDH-based materials can be extended to EL, CL, and ECL devices due to the uniform dispersion of photoactive molecules in 2D confined microenvironment supported by the superlattice structure of the multilayer films.

7 Conclusion and Outlook

In conclusion, LDH-based compounds have become promising photofunctional materials, which can be used in infrared radiation absorption, ultraviolet shielding, and tunable color/luminescence with both static and dynamic manners. Due to their inherent high stability, ion-exchangeable property, and tailorable photo-related performance, LDHs can serve as an effective building block to incorporate photoactive molecules for the fabrication of new hybrid materials with diverse potential applications. Through the adjustment of the elemental composition, charge density, and particle size of LDH precursors, the quantity and distribution of confined guests can be tuned, which enable the fabrication of photofunctional materials with preferred orientations. Host–guest interaction and interlayer confinement effect can further influence the arrangement and orientation of intercalated guest molecules, and hybrid materials with superior optical properties compared with the pristine form can be achieved. For example, the LDH-based luminescent materials with precisely tuned emission in the whole visible range are obtained. And the hybrid materials also present repeatable and reversible responses toward external stimuli (such as light, pH, pressure, temperature, electricity, and chemicals), which can be utilized in the fields of photochromic, piezochromic, thermochromic, and polarized luminescence, chemical sensors, and switches. Moreover, some of LDHs systems (IR absorption and UV-shielding materials) have already been used as functional additives due to the significant improvement of IR/UV properties for polymers and asphalt.

From both academic and engineering perspectives, two key scientific problems still need to be further understood for these LDH-based photofunctional materials: (1) How the fine structures in both the inner layer and interlayer of LDHs (such as interface, surface, and defect) as well as their size effect can influence the macroscopical photo-related properties; (2) how the host–guest interactions between the LDHs layers and photoactive guests can influence the arrangement, orientation, and aggregation of the interlayer species. In addition, to meet the need of practical application, further explorations and interests can be concentrated on: (1) Intelligent materials: the development of new types of stimuli-responsive luminescent materials with fast response, high on/off ratio, and good repeatability

are highly desirable. As well, the multi-stimuli-responsive materials remain in an early stage and have been very seldom studied. (2) Large-scale preparation of LDHs photofunctional materials: up to now, most of these materials are still at the laboratory level, and how to scale up the LDHs materials for industrial applications needs further exploration from both process engineering and product engineering perspectives. (3) Combination of the photo-related performance with other functionalities, such as medical, pharmaceutical, environment, and energy fields, would be an important strategy and direction to broaden LDH-based multifunctional materials. Researches in these directions are continuing by us and many others worldwide.

Acknowledgment We would like to thank all the coworkers cited in the references for their invaluable contributions to the work described here. This work was supported by the 973 Program (Grant No. 2014CB932103), the National Natural Science Foundation of China (NSFC), Beijing Municipal Natural Science Foundation (Grant No. 2152016), the 111 Project (Grant B07004), and Program for Changjiang Scholars and the Innovative Research Team in University (PCSIRT: IRT1205).

References

1. Newman SP, Jones W (1998) *New J Chem* 22:105
2. Funnell NP, Wang Q, Connor L, Tucker MG, O'Hare D, Goodwin AL (2014) *Nanoscale* 6:8032
3. Jellicoe TC, Fogg AM (2012) *J Phys Chem Solids* 73:1496
4. Fogg AM, Dunn JS, Shyu SG, Cary DR, O'Hare D (1998) *Chem Mater* 10:351
5. Wang Q, O'Hare D (2012) *Chem Rev* 112:4124
6. Ma R, Liu Z, Li L, Iyi N, Sasaki T (2006) *J Mater Chem* 16:3809
7. He J, Wei M, Li B, Kang Y, Evans DG, Duan X (2006) *Struct Bond* 119:89
8. Kim JA, Hwang SJ, Choy JH (2008) *J Nanosci Nanotechnol* 8:5172
9. Guo X, Zhang F, Evans DG, Duan X (2010) *Chem Commun* 46:5197
10. Liu Z, Ma R, Osada M, Iyi N, Ebina Y, Takada K, Sasaki T (2006) *J Am Chem Soc* 128:4872
11. Evans DG, Slade RCT (2006) *Struct Bond* 119:1
12. Yan D, Lu J, Duan X (2013) *Scientia Sinica Chimica* 43:1
13. Li C, Dou Y, Liu J, Chen Y, He S, Wei M, Evans DG, Duan X (2013) *Chem Commun* 49:9992
14. Shao M, Ning F, Zhao J, Wei M, Evans DG, Duan X (2012) *J Am Chem Soc* 134:1071
15. Vialat P, Leroux F, Taviot-Gueho C, Villemure G, Mousty C (2013) *Electrochim Acta* 107:599
16. Choi SJ, Choy JH (2011) *Nanomedicine* 6:803
17. Yan D, Lu J, Wei M, Evans DG, Duan X (2011) *J Mater Chem* 21:13128
18. Gursky JA, Blough SD, Luna C, Gomez C, Luevano AN, Gardner EA (2006) *J Am Chem Soc* 128:8376
19. Gardner E, Huntoon KM, Pinnavaia TJ (2001) *Adv Mater* 13:1263
20. Li C, Wang L, Wei M, Evans DG, Duan X (2008) *J Mater Chem* 18:2666
21. Wang L, Li C, Liu M, Evans DG, Duan X (2007) *Chem Commun* 2:123
22. Zhang F, Sun M, Xu S, Zhao L, Zhang B (2008) *Chem Eng J* 141:362
23. Han J, Dou Y, Wei M, Evans DG, Duan X (2010) *Angew Chem Int Ed* 49:2171
24. Dou Y, Han J, Wang T, Wei M, Evans DG, Duan X (2012) *J Mater Chem* 22:14001

25. Zhang Z, Chen G, Xu K (2013) *Ind Eng Chem Res* 52:11045
26. Xu K, Zhang Z, Chen G, Shen J (2014) *RSC Adv* 4:19218
27. Posati T, Costantino F, Latterini L, Nocchetti M, Paolantoni M, Tarpani L (2012) *Inorg Chem* 51:13229
28. Zhao Y, Li JG, Fang F, Chu N, Ma H, Yang X (2012) *Dalton Trans* 41:12175
29. Gunawan P, Xu R (2009) *J Phys Chem C* 113:17206
30. Gao X, Hu M, Lei L, O'Hare D, Markland C, Sun Y, Faulkner S (2011) *Chem Commun* 47:2104
31. Gao X, Lei L, Kang L, Wang Y, Lian Y, Jiang K (2014) *J Alloys Compd* 585:703
32. Zhang Z, Chen G, Liu J (2014) *RSC Adv* 4:7991
33. He Q, Yin S, Sato T (2004) *J Phys Chem Solids* 65:395
34. Shi W, Lin Y, Zhang S, Tian R, Liang R, Wei M, Evans DG, Duan X (2013) *Phys Chem Chem Phys* 15:18217
35. Tuo Z (2006) Beijing University of Chemical Technology, China
36. Chai H (2008) Beijing University of Chemical Technology, China
37. Yu S, Zheng Y, Du J, Liu J, Shang H, Liu L (2005) *China Surf Det Cosm* 352:48
38. Xing Y (2003) Beijing University of Chemical Technology, China
39. Xing Y, Li D, Guo C, Evans DG, Duan X (2003) *Fine Chem* 20:1
40. Wang G, Rao D, Li K, Lin Y (2014) *Ind Eng Chem Res* 53:4165
41. Xing Y, Li D, Reng L, Evans DG, Duan X (2003) *Acta Chim Sin* 61:267
42. Zhang L, Lin Y, Tuo Z, Evans DG, Li D (2007) *J Solid State Chem* 180:1230
43. Cui G, Evans DG, Li D (2010) *Polym Degrad Stab* 95:2082
44. Cui GJ, Xu XY, Lin YJ, Evans DG, Li DQ (2010) *Ind Eng Chem Res* 49:448
45. Feng Y, Li D, Wang Y, Evans DG, Duan X (2006) *Polym Degrad Stab* 91:789
46. Li D, Tuo Z, Evans DG, Duan X (2006) *J Solid State Chem* 179:3114
47. Sun W, He Q, Luo Y (2007) *Mater Lett* 61:1881
48. Lin Y, Tuo Z, Chai H, Evans DG, Li D (2006) *Chin J Inorg Chem* 22:1431
49. Chai H, Lin Y, Evans DG, Li D (2008) *Ind Eng Chem Res* 47:2855
50. Chai H, Xu X, Lin Y, Evans DG, Li D (2009) *Polym Degrad Stab* 94:744
51. Zhu H, Feng Y, Tang P, Cui G, Evans DG, Li D, Duan X (2011) *Ind Eng Chem Res* 50:13299
52. Wang J (2012) Beijing University of Chemical Technology, China
53. Wang L, Xu X, Evans DG, Li D (2010) *Ind Eng Chem Res* 49:5339
54. Liu Y (2002) *Plastics Sci Technol* 2:22
55. Wang L, Wang L, Feng Y, Feng J, Li D (2011) *Appl Clay Sci* 53:592
56. Gao J (1999) *China Plast* 13:66
57. Ding S (1998) *Chin Synth Res Plast* 15:32
58. Tian Y (2004) *China Plast* 18:1
59. Zhu H, Tang P, Feng Y, Wang L, Li D (2012) *Mater Res Bull* 47:532
60. Wang S, Zhao X, Li SL (2003) *Plast Sci Technol* 3:29
61. Kunihiko K (2003) *China Plast* 17:1
62. Wang L, Xu X, Evans DG, Duan X, Li D (2010) *J Solid State Chem* 183:1114
63. Jiao Q, Zhao Y, Xie H, Evans DG, Duan X (2002) *Chin J Appl Chem* 19:1011
64. Xie H (2000) Beijing University of Chemical Technology, China
65. Liu J, Lian S, Zhu A, Li Q, Liu L, Zeng L (2007) *Chin J Lumin* 28:67
66. Duan X, Lu J (2013) *Nano science and technology. The two-dimensional nano composite hydroxide: structure, assembly and function.* Science Press, China
67. Chen Z, Kang J (2006) *China Plast* 20:13
68. Wang L, Cui H, Jiao H (2007) *Spectrosc Spect Anal* 27:259
69. Wang L, Xu X, Evans DG, Li D (2010) *Chin J Inorg Chem* 26:970
70. Wang L (2011) Beijing University of Chemical Technology, China
71. Badreddinea M, Legrouiri A, Barroug A, DeRoy A, Besse JP (1999) *Mater Lett* 38:391
72. Xu G, Guo C, Duan X (1999) *Chin J Appl Chem* 16:45

73. Haurie L, Fernández AI, Velasco JI, Chimenos JM, Lopez Cuesta JM, Espiell F (2006) *Polym Degrad Stab* 91:989
74. Roy PK, Surekha P, Rajagopal C, Chatterjee SN, Choudhary V (2007) *Polym Degrad Stab* 92:1151
75. Singh R, Samra KS, Kumar R, Singh L (2008) *Radiat Phys Chem* 77:53
76. Yan D, Lu J, Wei M, Han J, Ma J, Li F, Evans DG, Duan X (2009) *Angew Chem Int Ed* 48:3073
77. Yan D, Lu J, Wei M, Qin S, Chen L, Zhang S, Evans DG, Duan X (2011) *Adv Funct Mater* 21:2497
78. Yan D, Lu J, Ma J, Wei M, Wang X, Evans DG, Duan X (2010) *Langmuir* 26:7007
79. Yan D, Lu J, Ma J, Wei M, Evans DG, Duan X (2011) *AIChE J* 57:1926
80. Gao R, Lei X, Chen M, Yan D, Wei M (2013) *New J Chem* 37:4110
81. Shi W, Lin Y, He S, Zhao Y, Li C, Wei M, Evans DG, Duan X (2011) *J Mater Chem* 21:11116
82. Han J, Yan D, Shi W, Ma J, Yan H, Wei M, Evans DG, Duan X (2010) *J Phys Chem B* 114:5678
83. Yan D, Lu J, Wei M, Ma J, Evans DG, Duan X (2009) *Chem Commun* 42:6358
84. Li S, Lu J, Ma H, Xu J, Yan D, Wei M, Evans DG, Duan X (2011) *Langmuir* 27:11501
85. Li S, Lu J, Wei M, Evans DG, Duan X (2010) *Adv Funct Mater* 20:2848
86. Li S, Lu J, Xu J, Dang S, Evans DG, Duan X (2010) *J Mater Chem* 20:9718
87. Li S, Lu J, Ma H, Yan D, Li Z, Qin S, Evans DG, Duan X (2012) *J Phys Chem C* 116:12836
88. Daniel SR, Prabir KD (1996) *Langmuir* 12:402
89. Eva K, Kamil L, Pavel K, Mariana K, Jiří M, Miroslav Š, Anne-Lise TT, Fabrice L, Vincent V, Christine TG (2010) *J Mater Chem* 20:9423
90. Eva K, Christine TG, Petr B, Mariana K, Petr K, Pavel K, Jiří M, Miroslav P, Kamil L (2010) *Chem Mater* 22:2481
91. Marie J, Jan D, Pavel K, Jiří H, František K, Kamil L (2011) *J Phys Chem C* 115:21700
92. Liang R, Tian R, Ma L, Zhang L, Hu Y, Wang J, Wei M, Yan D, Evans DG, Duan X (2014) *Adv Funct Mater* 24:3144
93. Qin Y, Lu J, Li S, Li Z, Zheng S (2014) *J Phys Chem C* 118:20538
94. Yan D, Lu J, Wei M, Evans DG, Duan X (2009) *J Phys Chem B* 113:1381
95. Yan D, Lu J, Chen L, Qin S, Ma J, Wei M, Evans DG, Duan X (2010) *Chem Commun* 46:5912
96. Yan D, Lu J, Wei M, Ma J, Evans DG, Duan X (2009) *Phys Chem Chem Phys* 11:9200
97. Zhang Y, Song M, Yun R, Meng Q, Yan D (2014) *Chin J Chem* 32:859
98. Yan D, Lu J, Ma J, Wei M, Evans DG, Duan X (2010) *Phys Chem Chem Phys* 12:15085
99. Yan D, Lu J, Ma J, Wei M, Evans DG, Duan X (2011) *Angew Chem Int Ed* 50:720
100. Yan D, Lu J, Ma J, Wei M, Li S, Evans DG, Duan X (2011) *J Phys Chem C* 115:7939
101. Yan D, Lu J, Wei M, Li S, Evans DG, Duan X (2012) *Phys Chem Chem Phys* 14:8591
102. Tian R, Liang R, Yan D, Shi W, Yu X, Wei M, Li LS, Evans DG, Duan X (2013) *J Mater Chem C* 1:5654
103. Ma H, Gao R, Yan D, Zhao J, Wei M (2013) *J Mater Chem C* 1:4128
104. Shi W, Wei M, Lu J, Li F, He J, Evans DG, Duan X (2008) *J Phys Chem C* 112:19886
105. Shi W, Wei M, Lu J, Evans DG, Duan X (2009) *J Phys Chem C* 113:12888
106. Shi W, He S, Wei M, Evans DG, Duan X (2010) *Adv Funct Mater* 20:3856
107. Shi W, Sun Z, Wei M, Evans DG, Duan X (2010) *J Phys Chem C* 114:21070
108. Shi W, Ji X, Zhang S, Wei M, Evans DG, Duan X (2011) *J Phys Chem C* 115:20433
109. Shi W, Ji X, Wei M, Evans DG, Duan X (2012) *Langmuir* 28:7119
110. Yan D, Lu J, Ma J, Wei M, Qin S, Chen L, Evans DG, Duan X (2010) *J Mater Chem* 20:5016
111. Yan D, Lu J, Ma J, Qin S, Wei M, Evans DG, Duan X (2011) *Angew Chem Int Ed* 50:7037
112. Wang X, Lu J, Shi W, Li F, Wei M, Evans DG, Duan X (2010) *Langmuir* 26:1247
113. Shi W, Lin Y, Kong X, Zhang S, Jia Y, Wei M, Evans DG, Duan X (2011) *J Mater Chem* 21:6088

114. Yan D, Zhao Y, Wei M, Liang R, Lu J, Evans DG, Duan X (2013) *RSC Adv* 3:4303
115. Zheng S, Lu J, Li W, Qin Y, Yan D, Evans DG, Duan X (2014) *J Mater Chem C* 2:5161
116. Liang R, Tian R, Shi W, Liu Z, Yan D, Wei M, Evans DG, Duan X (2013) *Chem Commun* 49:969
117. Liang R, Xu S, Yan D, Shi W, Tian R, Yan H, Wei M, Evans DG, Duan X (2012) *Adv Funct Mater* 22:4940
118. Liang R, Yan D, Tian R, Yu X, Shi W, Li C, Wei M, Evans DG, Duan X (2014) *Chem Mater* 26:2595
119. Bendall JS, Paderi M, Ghigliotti F, Li Pira N, Lambertini V, Lesnyak V, Gaponik N, Visimberga G, Eychmüller A, Torres CMS, Welland ME, Gieck C, Marchese L (2010) *Adv Funct Mater* 20:3298
120. Dong S, Guan W, Lu C (2013) *Sens Actuators B Chem* 188:597
121. Dong S, Liu F, Lu C (2013) *Anal Chem* 85:3363
122. Cho S, Jung S, Jeong S, Bang J, Park J, Park Y, Kim S (2013) *Langmuir* 29:441
123. Cho S, Kwag J, Jeong S, Baek Y, Kim S (2013) *Chem Mater* 25:1071
124. Xu X, Zhang F, Xu S, He J, Wang L, Evans DG, Duan X (2009) *Chem Commun* 48:7533
125. Wu G, Wang L, Evans DG, Duan X (2006) *Eur J Inorg Chem* 2006:3185
126. Han Z, Guo Y, Tsunashima R, Song YF (2013) *Eur J Inorg Chem* 2013:1475
127. Omwomaa S, Chena W, Tsunashimab R, Song Y (2014) *Coord Chem Rev* 258–259:58–71
128. Sousa FL, Pillinger M, Sá Ferreira RA, Granadeiro CM, Cavaleiro AMV, Rocha J, Carlos LD, Trindade T, Nogueira HIS (2006) *Eur J Inorg Chem* 2006:726
129. Li L, Ma R, Ebina Y, Iyi N, Sasaki T (2005) *Chem Mater* 17:4386
130. Ma RZ, Sasaki T (2012) *Recent Pat Nanotechnol* 6:159
131. Takakazu Y, Kiyoshi S, Takashi K, Tetsuji I, Takaki K (1996) *J Am Chem Soc* 118:3930
132. Siringhaus H (2005) *Adv Mater* 17:2411
133. Igor AL, Jinsang K, Timothy MS (1999) *J Am Chem Soc* 121:1466
134. Gao ZQ, Mi BX, Tam HL, Cheah KW, Chen CH, Wong MS, Lee ST, Lee CS (2008) *Adv Mater* 20:774
135. Li Z, Lu J, Li S, Qin S, Qin Y (2012) *Adv Mater* 24:6053
136. Shi W, Wei M, Evans DG, Duan X (2010) *J Mater Chem* 20:3901
137. Sun Z, Jin L, Shi W, Wei M, Evans DG, Duan X (2011) *Langmuir* 27:7113
138. Yan D, Lu J, Wei M, Evans DG, Duan X (2013) *Chem Eng J* 225:216
139. Ray K, Nakahara H (2002) *J Phys Chem B* 106:92
140. Wood V, Panzer MJ, Chen J, Bradley MS, Halpert JE, Bawendi MG, Bulovic V (2009) *Adv Mater* 21:1
141. Kim S, Kim T, Kang M, Kwak SK, Yoo TW, Park LS, Yang I, Hwang S, Lee JE, Kim SK, Kim SW (2012) *J Am Chem Soc* 134:3804
142. Lee M, Yang R, Li C, Wang ZL (2010) *J Phys Chem Lett* 1:2929
143. Chiang CL, Tseng SM, Chen CT, Hsu CP, Shu CF (2008) *Adv Funct Mater* 18:248
144. Shang M, Geng D, Kang X, Yang D, Zhang Y, Lin J (2012) *Inorg Chem* 51:11106
145. Wang M, Guo S, Li Y, Cai L, Zou J, Xu G, Zhou W, Zheng F, Guo G (2009) *J Am Chem Soc* 131:13572
146. Ki W, Li J (2008) *J Am Chem Soc* 130:8114
147. Kwak J, Bae WK, Lee D, Park I, Lim J, Park M, Cho H, Woo H, Yoondo Y, Char K, Lee S, Lee C (2012) *Nano Lett* 12:2362
148. Rosson TE, Claiborne SM, McBride JR, Stratton BS, Rosenthal SJ (2012) *J Am Chem Soc* 134:8006
149. Gao R, Zhao M, Guan Y, Fang X, Li X, Yan D (2014) *J Mater Chem C* 2:9579
150. Kim HN, Guo Z, Zhu W, Yoon J, Tian H (2011) *Chem Soc Rev* 40:79
151. Li W, Yan D, Gao R, Lu J, Wei M, Duan X (2013) *J Nanomater* 2013:437082
152. Tomchenko AA, Harmer GP, Marquis BT (2005) *Sens Actuators B* 108:41
153. Davis AP, Wareham RS (1999) *Angew Chem Int Ed* 38:2978

154. Zampolli S, Elmi I, Ahmed F, Passini M, Cardinali GC, Nicoletti S, Dori L (2005) *Sens Actuators B* 105:400
155. Yoon S, Miller EW, He Q, Do PH, Chang CJ (2007) *Angew Chem Int Ed* 46:6658
156. Rose A, Hu Z, Madigan CF, Swager TM, Bulovic V (2005) *Nature* 434:876
157. Sun Z, Jin L, Zhang S, Shi W, Pu M, Wei M, Evans DG, Duan X (2011) *Anal Chim Acta* 702:95
158. Jin L, Guo Z, Wang T, Wei M (2013) *Sens Actuators B* 177:145
159. Jin L, Guo Z, Sun Z, Li A, Jin Q, Wei M (2012) *Sens Actuators B* 161:714
160. Michelle M, Ward M, Asher SA (2008) *Adv Funct Mater* 18:1186
161. Schroeder CR, Weidgans BM, Klimant I (2005) *Analyst* 130:907
162. Mattu J, Johansson T, Holdcroft S, Leach GW (2006) *J Phys Chem B* 110:15328
163. Roy I, Gupta MN (2003) *Chem Biol* 10:1161
164. Chandrasekharan N, Kelly LA (2001) *J Am Chem Soc* 123:9898
165. Allison SW, Gillies GT (1997) *Rev Sci Instrum* 68:2615
166. Tian L, He F, Zhang H (2007) *Angew Chem Int Ed* 46:3245
167. Kunzelman J, Kinami M, Crenshaw BR, Protasiewicz JD, Weder C (2008) *Adv Mater* 20:119
168. Zhang X, Chi Z, Li H (2011) *Chemistry* 6:808
169. Chi Z, Zhang X, Xu B (2012) *Chem Soc Rev* 41:3878
170. Zhao Y, Lin H, Chen M, Yan D (2014) *Ind Eng Chem Res* 53:3140
171. Durr H (1989) *Angew Chem Int Ed* 28:413
172. Zhang J, Zou Q, Tian H (2012) *Adv Mater* 25:378
173. Fukaminato T, Irie M (2006) *Adv Mater* 18:3225
174. Wang X, Lu J, Yan D, Wei M, Evans DG, Duan X (2010) *Chem Phys Lett* 493:333
175. Jan D, Kamil L (2012) *Eur J Inorg Chem* 2012:5154
176. Schreuder MA, Xiao K, Ivanov IN, Weiss SM, Rosenthal SJ (2010) *Nano Lett* 10:573
177. Gill SK, Brice LK (1984) *J Chem Educ* 61:713
178. Richter MM (2004) *Chem Rev* 104:3003
179. Zhang B, Shi S, Shi W, Sun Z, Kong X, Wei M, Duan X (2012) *Electrochim Acta* 67:133